"In our tenure on this planet we've accumulated dangerous evolutionary baggage propensities for aggression and ritual, submission to leaders, hostility to outsiders all of which puts our survival in some doubt. But we've also acquired compassion for others, love for our children and desire to learn from history and experience, and a great soaring passionate intelligence – the clear tools for our continued survival and prosperity."

Carl Sagan

University of Alberta

Characterization of In-line Holographic Point Projection Microscope

by

Aaron Peter Legg

A thesis submitted to the Faculty of Graduate Studies and Research
in partial fulfillment of the requirements for the degree of

Master of Science

Department of Physics

Fall 2013
Edmonton, Alberta

To my family, who taught me to strive to be more;
and my mentors, who gave me the opportunity.

Abstract

To overcome the limitations of lens aberrations in an electron microscope, Dr. Dennis Gabor invented electron holography, a technique that uses no lenses. The technique uses low energies (60-200eV), which makes it ideal for imaging fragile biological samples. To suspend samples, graphene has been employed. Electron holography was initially limited by the source of coherent electrons.

New field-emission sources have shown the required coherence for high resolution electron holography. Previously, tungsten(110) polycrystalline tips were used as a source. Using a graphene knife edge, I compare new tungsten(111) single crystalline hybrid tips as an alternative due to their stability during etching. During the knife edge experiment, I noticed small defects on the surface of the film. I was able to obtain a high resolution measurement of 6.8 Å.

New standard samples, such as gold on graphene, must be explored to increase our understanding of the resolution of an electron holography microscope.

Acknowledgements

First I'd like to thank Dr. Robert Wolkow. When I first arrived in Edmonton I was just a young man with a drive to give back to the community. With Dr. Wolkow's guidance I was able to transform from that young man into a scientist. Thank you for giving me the opportunity to repay the world of physics.

I'd like to thank Dr. Lucian Livadaru for teaching me about the theory of holography and for always making himself available. I would also like to thank him for writing the reconstruction algorithm used in this thesis.

Much of the computer programs and my understanding of CCD cameras comes from long informative discussions with Dr. Radovan Urban. Thank you for helping me learn labview and providing me with the knowledge I needed.

I'd also like to thank Dr. Josh Mutus, for building the machine that made my thesis possible and for helping me from a great distance with troubleshooting different experimental parameters.

I'd like to thank our research group for providing insight and support along the way: Martin Cloutier, Mark Salomons, Marco Taucer, Jason Pitters, Paul Piva, Roshan Achal, Taleana Huff, Hatem Labidi, Bruno Martins, Shoma Sinha, Christian Vesa, Stas Dogel, Gino DiLabio and Peter Ryan.

Finally, I'd like to thank my family and friends for supporting me through these last few years. Especially my mother and father who became my source of confidence and reassurance. Thank you so much for all that you have given me.

Table of Contents

List of Figures

List of Tables

Chapter 1

Introduction

1.1 The Invention of holography

During Ernst Abbe's impressive career, he was able to identify a hard limit on the resolution of a microscope. The limit depends on two parameters, wavelength and the focal length. The maximum resolution of a diffraction limited microscope is given by:

$$d = \frac{\lambda}{2(n \sin \theta)}, \tag{1.1}$$

where λ is the wavelength and $n \sin \theta$ is the numerical aperture (NA) (figure 1.1). Using this definition, an optical microscope using conventional lenses is limited to a resolution of 200 nm. Due to the limited applicability of high NA components, the simplest way to increase resolution is to tune the source's wavelength.

To decrease the wavelength of the source, Ernst Ruska and Max Knoll built the first electron microscope in 1931.[1] The electron wavelenth is given by the de Boglie equation,

$$\lambda = \frac{h}{\sqrt{(2m_e E)}}, \tag{1.2}$$

where h is Planck's constant, m_e is the mass of an electron and E is the electron energy in eV. By increasing the energy of the electron, the wavelength can be made smaller, which enables it to probe smaller features. The microscope used electromagnetic and electrostatic lenses to focus the beam. This system, which had the potential to reach very high resolution, was limited by the aberrations caused by the quality of the lenses [2]. Dennis Gabor discussed these limitations in his book *The Electron Microscope*, in the concluding chapter, titled "The ultimate limit of electron microscopy" [3].

To circumvent the resolution-limiting aberrations, Gabor invented a two-stage imaging technique he called "microscopy by reconstructed wavefronts". The idea was to create an intermediate image, which he called a hologram, using electron optics which would suffer from the same aberrations as the electron microscope. The second step of the process would remove aberrations, using light optics, which would result in high resolution images [3].

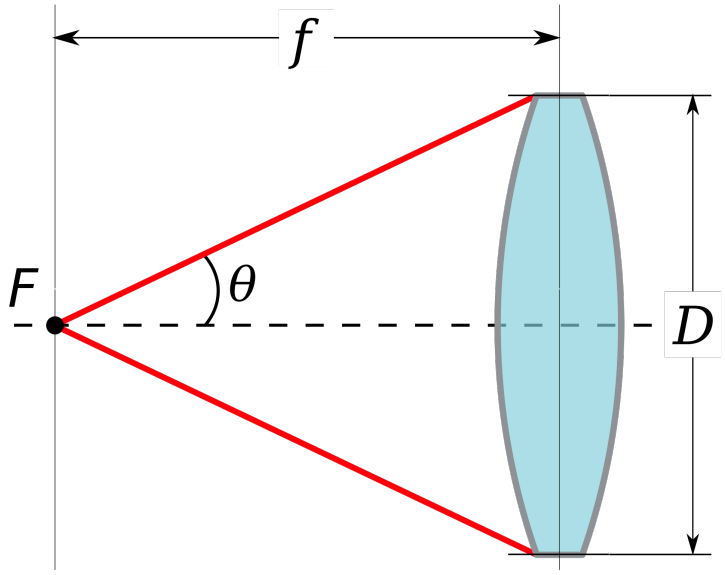

Figure 1.1: The numerical aperture (NA) of a lens is defined by the sine of half of the opening angle of the lens times the index of refraction. The angle is measured from the focal point, F. Reproduced from the Wikimedia Commons.

As Gabor recalls, the idea, which came to him while waiting for a tennis court in 1947, was inspired by two things: an understanding of Huygens' Principle (the idea that a wavefront can be reconstructed by summing an infinite number of point sources, which will be discussed later in this thesis) and his reading of Abbe's *Theory of the Microscope* [3].

> When we take a photograph, the image appears in the plane of the plate. But by Huygens' Principle the information which goes into the image must be there in every plane. [3]

Gabor conducted the first holography experiments himself[4]. Limited by the electron sources available, Gabor used an optical system to show proof of the concept of his invention. Gabor obtained both a hologram and a reconstruction in a single instrument. Figure 1.2 shows the results of using light to create a hologram [4]. Gabor explains in his paper that the poor quality of the reconstruction was due to the optics in the system [3].

Despite its energetic announcement and support from Sir Lawrence Bragg, holography did not catch on in the scientific community. The process was described as unintuitive and baffling. Even amongst the researchers in the field it was considered to be a "white elephant" and limited to a specific area of research. Gabor, unable to successfully convince the scientific community of holography's potential, had no choice but to abandon the study[3].

The technique had two seemingly insurmountable limitations. First, no source of coherent electrons existed to create high-resolution holograms. The available sources were also unable to emit with high intensity, which caused information to be lost to noise. Secondly,

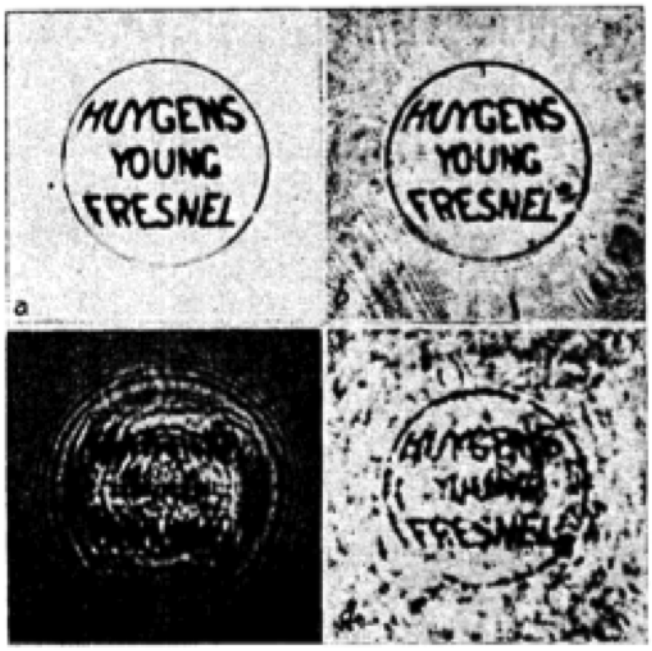

Figure 1.2: First hologram and reconstruction ever obtained by Dennis Gabor. Hologram in c) was created using an arc-discharge lamp to illuminate a transparency shown in a). The reconstruction of the hologram is shown in d).[4]

the microscope produced a twin image, an out-of-focus conjugate image that obstructed the reconstruction in the fresnel (near field) regime.[3]

Holography, however, was not completely abandoned. Research was being conducted in classified projects on the topic of wavefront reconstruction in both the United States and Soviet Russia. State side, Emmett Leith and Juris Upatnieks worked together to develop their own holographic microscope which employed an off-axis reference beam which allowed the twin and real images to be isolated geometrically.[3] This, and the invention of the laser, allowed Leith and Upatnieks to explore holography and promote it in a way Gabor had not been able to, as a technique which yielded real results. The research done by Leith and Upatnieks led to Gabor winning the Nobel Prize in 1971 for inventing holography.[5]

Despite Leith and Upatnieks great accomplishments, the long wavelength of their source prevented them from fulfilling Gabor's goal of surpassing the resolution limitations of the electron microscope. In 1968, A. V. Crewe presented a new method of creating electron sources[6, 7]. Crewe used an electrochemical process to create tungsten tips with a radius of curvature as small as 20 nm. Tungsten was used for its high melting point, low vapour pressure, high conductivity and mechanical strength.[7] By applying a voltage between the tip and the extractor, tungsten's work function can be overcome to produce a beam of electrons. The process was named cold field emission, to distinguish it from thermionic emitters. This new source of electrons was the brightest source to date[6, 7] and, thus, was able to solve one of holography's limitations. The tips, however, could not solve the

problem of limited coherence from an electron source.

To increase the coherence of the source, the size of the tip needed to be smaller than the tips Crewe created. In 1986, Hans-Werner Fink at IBM developed a technique that would allow the user to build on an etched tip. The tip would be imaged using field ion microscopy to observe its apex. Once the tip was clean, the process deposits a single tungsten atom at the end of the tip to create the first single atom tip (SAT). The SATs showed an increase in coherence and brightness[3, 8], which led to the revival of electron holography.

1.2 Electron Holography

The word hologram, coined by Gabor [3], is derived from Greek and means "whole picture". A hologram is the result of two interacting wavefronts, the reference and scattered waves, which create an interference pattern containing all of the information about the source and sample. The reference, a spherical wave of electrons which emanates from the source towards the sample and detector, is given by:

$$\Psi_{ref} = Re^{i\phi_{ref}}, \tag{1.3}$$

where R is the amplitude of the wave and ϕ_{ref} is the phase.

When the reference beam reaches the sample, it partially interacts with the sample as well as passing through unperturbed. The interacting electrons scatter from the sample toward the detector. The atoms of the sample become secondary sources, each with its own amplitude and phase shift. The scattered wave is given by:

$$\Psi_{scat} = Se^{i\phi_{scat}}, \tag{1.4}$$

Huygens' principle states that a known wavefront at a given time can be used to construct the wavefront at any subsequent time using an infinite sum of unoccluded point sources[2] (figure 1.3). This means that the combined wavefront exists in all planes between the sample and the detector (figure 1.4). The hologram captured on the detector is an intensity given by:

$$I_{holo} = |\Psi_{ref} + \Psi_{scat}|^2 = R^2 + S^2 + 2RS\cos(\phi_{scat} - \phi_{ref}), \tag{1.5}$$

On the right hand side of equation 1.5, the first two terms are the individual reference and scattered intensities, as if the beams did not interact. The third term is the hologram. To isolate the holographic term, as a first step, the reference beam is subtracted from I_{holo}. The scattered wave, however, is considered to be negligible since the samples are chosen to be weak scatterers[10].

Once a hologram is captured it must be reconstructed to obtain the final image. Originally, this was achieved through the use of optics[12] (figure 1.5). Today, digital capture and processing has become the main method of reconstruction.

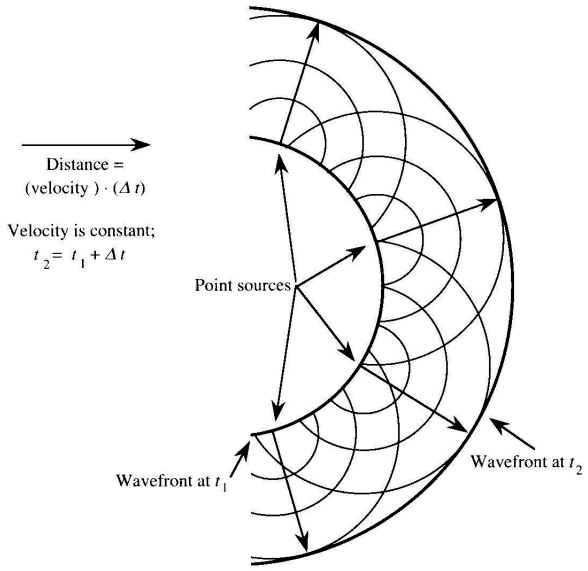

Figure 1.3: Huygens' Principle states that any wavefront, at a time t_2, can be constructed using an infinite number of points from a previous time slice of the wavefront. This means that the combined wavefront of a hologram exists in all planes. Reproduced from [9].

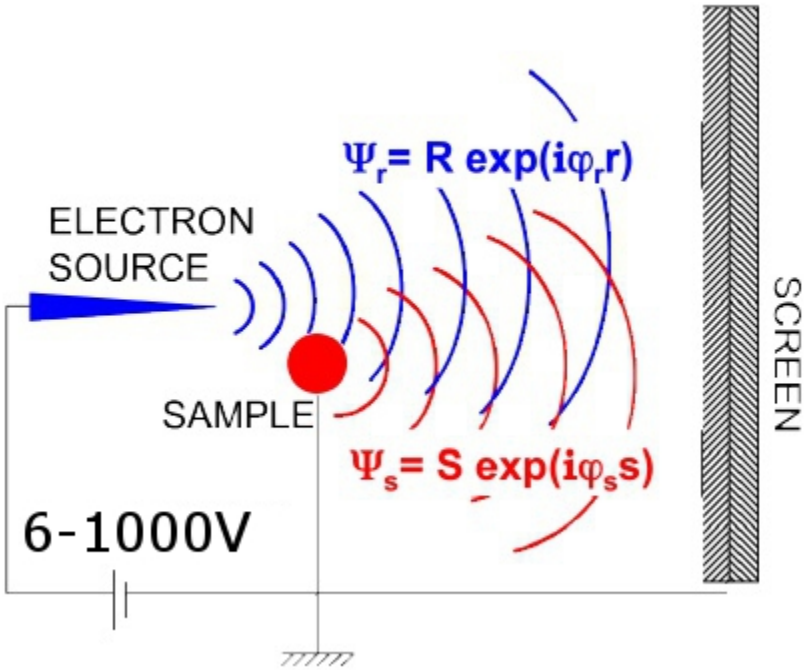

Figure 1.4: Schematic of the in-line lowe energy electron holographic technique. The reference wave (blue) propagates toward the sample and screen. The reference wave interacts with the sample to create a secondary wave called the scattered wave (red). The two waves interfere at the screen to create a hologram. [11]

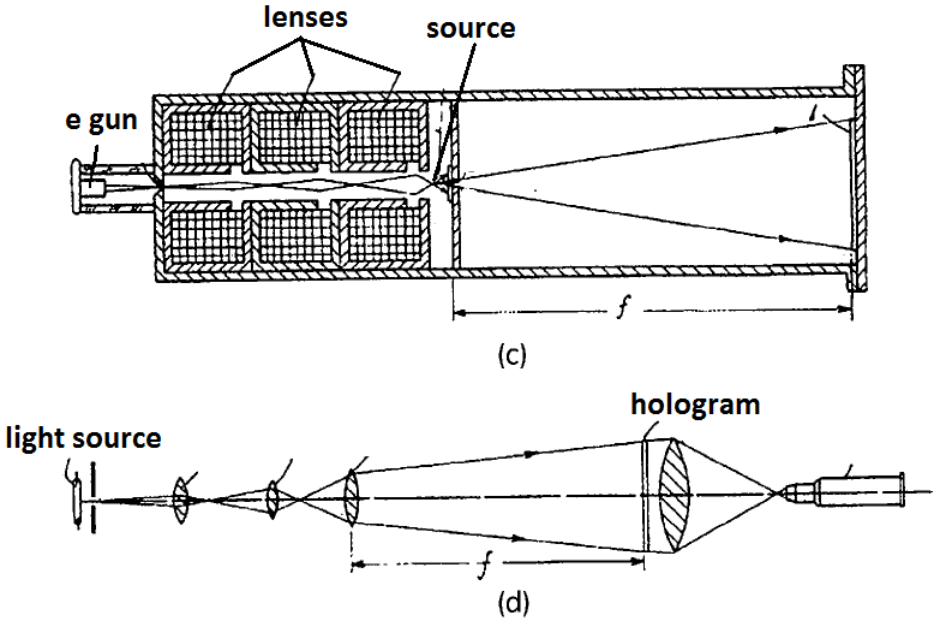

Figure 1.5: Schematic included in Gabor's original patent for electron holography. The system used electrons to capture the holograms and light to reconstruct. a) shows the electron gun and magnetic condenser lenses which focuses the beam to a single point. The point becomes the source of the microscope. An object is placed a small distance away to create a highly magnified hologram. b) is the reconstruction of the hologram using visible light. The hologram from a) is placed to the left of the final lens. [12]

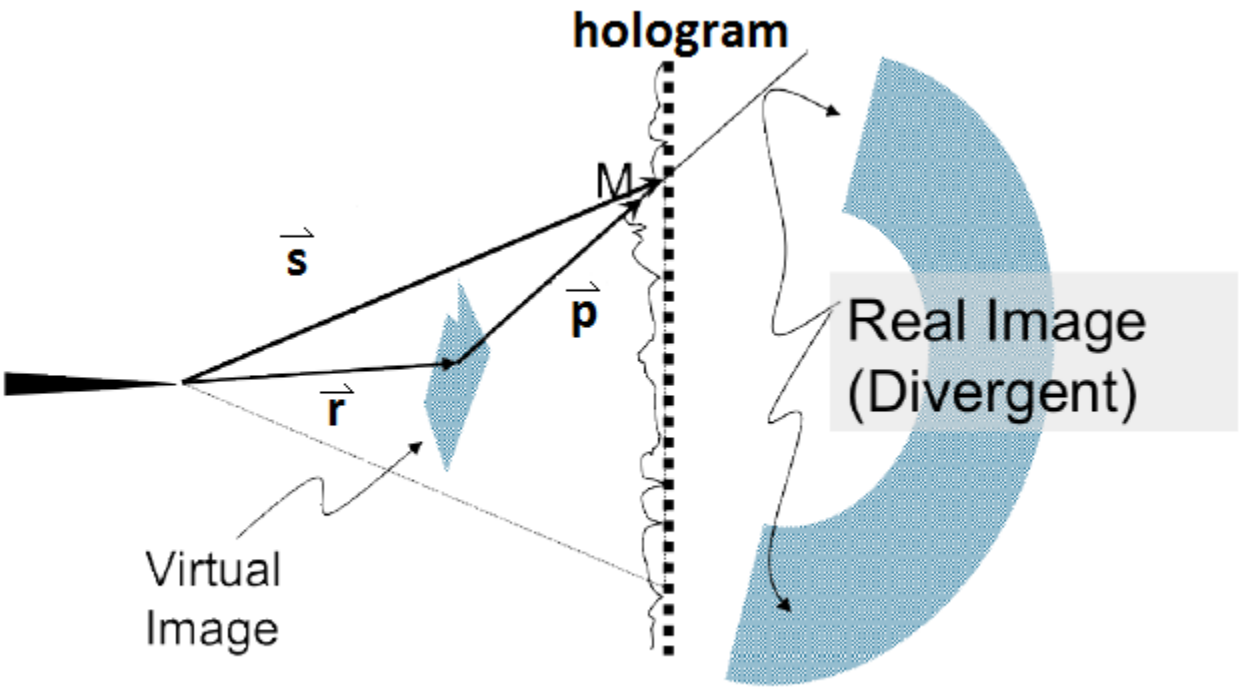

Figure 1.6: Schematic of the reconstruction process. The reference wave is reflected by the hologram with the intensity I_{holo} in the direction $\hat{p}$. The reflected wave then interacts with the new incoming reference wave to create the object a distance $\mathbf{r}$ from the source. To obtain the full reconstruction in some plane, a double integral over $\mathbf{s}$ and $\mathbf{r}$ is performed. [11]

A hologram can be reconstructed by numerically solving the Fresnel-Kirchoff integral in a process equivalent to back propagation of the wavefront[13]:

$$\psi(\mathbf{r}) = \int_{Screen} ds_x ds_y I_{holo}(\mathbf{s}) \frac{\exp(iks)}{s} \frac{\exp(-ik|\mathbf{r}-\mathbf{s}|)}{|\mathbf{r}-\mathbf{s}|}, \tag{1.6}$$

where I_{holo} is the intensity of the hologram given in equation 1.5 and k is the wave number of the beam. The vectors $\mathbf{s}$ and $\mathbf{r}$ are the lines between the source, or origin, to some point M on the detector and scatter site, respectively. In this process, the hologram, without the object present, is illuminated with the same wavefront that was used to create it. Figure 1.6 shows a view of a reconstruction process. The reference wave arrives at a point M on the hologram and is reflected. The intensity of the reflected wave depends on the value of I_{holo} at point M. The reflection causes an inversion of the wave back towards the source, characterized by $-(ik|\mathbf{r}-\mathbf{s}|)$, which then travels a distance $\mathbf{p}$ towards the plane of reconstruction. The solution is obtained when all values of $\mathbf{s}$ have been integrated for each $\mathbf{r}$ in a chosen object plane. Adjacent planes can be reconstructed to form a 3D image of the object.

The holographic microscope described above is an example of a lensless electron point projection microscope (PPM). A PPM is the simplest incarnation of a microscope which contains a source, a sample and a detector in series (figure 1.7). The field-emission source, a metal nano-tip terminating in a few atoms, illuminates the sample with a divergent beam resulting in a shadow image of the object on the detector. Using similar triangles, the magnification of a PPM is given by:

$$M = D/d, \tag{1.7}$$

where D is the source-to-detector distance and d is the source-to-sample distance. Since $D >> d$, D is often approximated as the sample-to-detector distance.

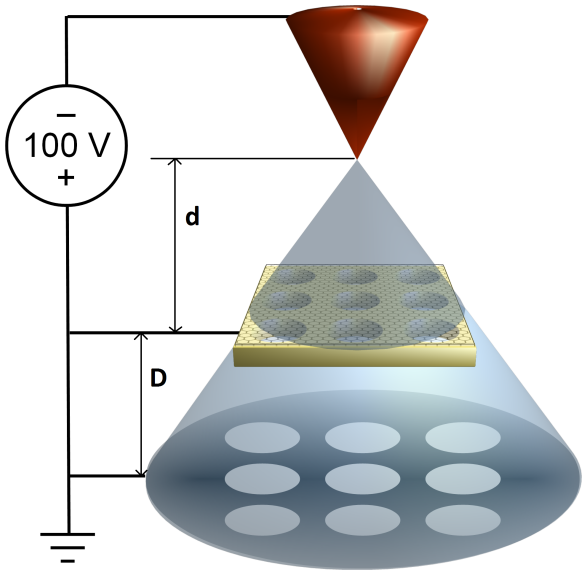

Figure 1.7: A typical PPM. The source emits a divergent beam of electrons towards a TEM grid coated in gold, which serves as the extractor, towards a distance detector. The beam projects a magnified shadow image of the sample onto the screen.[11]

To obtain a highly magnified image, the tip-to-sample distance, d must be small in comparison to the sample to detector distance, D, on the order of 100 nm. The most effective means of extracting electrons at these length scales is to use the sample to bias the tip. The extracting voltage defines the energy of the beam. The high curvature at the apex of the tip causes a high field at low biases[7]. Since low voltages are required to extract electrons from a tip and high voltages can damage it, the microscope uses low energy electrons in the range of 60 - 200 eV. Low energy electrons become highly attenuated by samples.[14] This leads to high contrast, but requires the samples be very thin.

Attenuation lengths can be estimated using:

$$I = I_0 \exp(-z/\lambda \cos\theta), \tag{1.8}$$

where I_0 is the initial irradiance, z is the thickness, λ is an attenuation parameter and θ is the angle from the perpendicular. The lower the energy of the source, the greater the attenuation of the beam will be. This imposes the requirement that the sample holder must be porous such that the electrons can pass through to the detector. To fulfill this requirement a transmission electron microscope (TEM) grid, which is an array of holes in a silicon nitride membrane, serves as a method to suspend the samples. The grid is coated with gold such that it can also collect electrons from the source, creating a divergent reference beam.

Low energy electrons also allow the microscope to avoid many types of damaging processes. The most straightforward form of damage is the displacement of atoms via a transfer of momentum from the incident electrons. This process is possible when the energy of the electron exceeds the displacement energy of the sample. For bulk atoms this process will cause the atom to move to an interstitial site, while surface atoms will be removed in a process known as sputtering [15]. Consider the TEM, which uses energies in the range of 20 - 200 keV. Figure 1.8 shows the sputtering rate of carbon atoms versus the energy of incoming electrons [15]. The rate, in mm/s, increases rapidly above $\approx$ 50keV. This process may also cause the sample to recrystallize, amorphize, or change its phase. Sample heating, which is thought to decrease with increasing beam energy, results from an inelastic process.[15] Sample heating is not usually an issue for metals, though it can be harmful to biological samples as it can lead to denaturing. Hydrocarbon surface contamination can also be an issue. Incoming electrons can polymerize hydrocarbon molecules, which have a low surface mobility and vapor pressure. This leads to a buildup of unwanted hydrocarbons on the surface of the sample.[15] Low energies, however, limit the resolution of the microscope due to the diffraction limit.

The resolution, which is defined as the minimum distance between points on an object that can be differentiated, is one of the most important aspects of a microscope. The minimum change in contrast for an object to be considered as two separate objects is 36%, as defined by the Rayleigh criterion (figure 1.9). In a typical electron microscope the resolution is limited by the wavelength of the electrons, the numerical aperture of the lenses and their aberration. A holographic projection microscope, which contains no lenses, is then only limited by the wavelength of the electrons used to illuminate the sample. This, however, is not the entire picture. The microscope is also limited by the coherence of the electrons emitted from the source.

To understand the dependence of the resolution on the coherence of the source, consider the case where a wave is occluded by a single point. When the reference wave interacts with the point, it creates a new point of illumination. The resulting hologram is a series of annuli of alternating brightness, known as a zone plate (figure 1.10). A zone plate is a lens that does not use different indices of refraction or surface shape to achieve focusing[17]. Since an object can be considered as an array of point scatterers, a hologram can then be

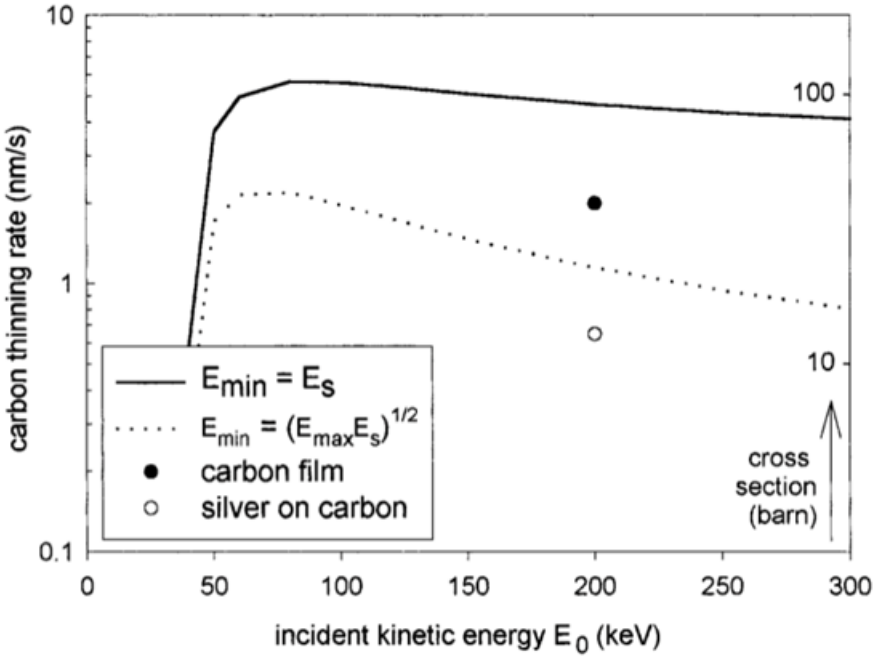

Figure 1.8: Plot of carbon sputtering (in mm/s) for a range of energies in TEM. The sputter rate tapers off at 60 keV, which corresponds to a wavelength of 0.05 Å. Low energy electron holography uses energies well below this threshold (1 Å), which leads to much lower sputter rates. [15]

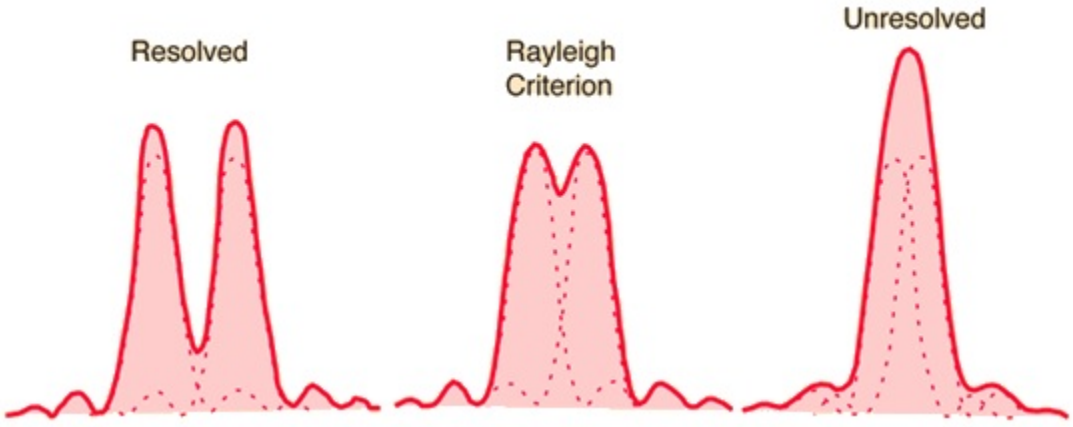

Figure 1.9: The Rayleigh Criterion describes the ability of a detector to differentiate between two points separated by a distance d. For coherent light, the minimum dip in contrast must be at least 36% of the maximum value. Reproduced from [16]

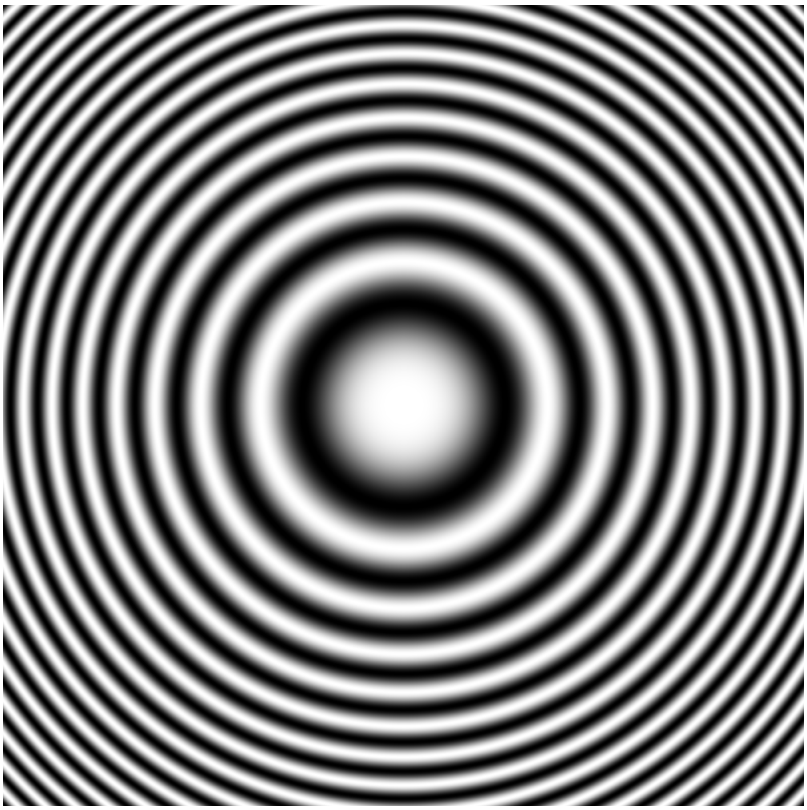

Figure 1.10: Fresnel zone plate. A lens created from alternating black and white "zones" to focus light. A zone plate is analogous to a hologram of a single point, thus a hologram can be thought of as a lens. Thus, the extent of a hologram can be used to calculate the resolution of the system. Reproduced with permission from the Wikimedia Commons.

thought of as a sum of individual zone plates, which itself is a zone plate. The hologram can then be considered to be a lens in the reconstruction process in which the NA is the half width of the pattern. Therefore, larger holograms correspond to higher spatial frequencies and therefore to higher resolutions[10]. The lateral extent of a hologram depends on the coherence of the interfering light.

1.2.1 Coherence

Coherence is the measure of the correlation of the phase in a wavefront. A coherent source emits a wave of a constant phase. In holography, if no coherent source is present, the reference and scattered wave will interfere in a random way such that details will be lost[18]. To understand coherence, consider two interacting waves with the same frequency ω. The field at any given point is a superposition of the two waves:

$$\mathbf{E} = \mathbf{E_1} + \mathbf{E_2}, \tag{1.9}$$

where

$$E_1 = A \exp i(k \cdot \mathbf{r} - \omega t + \phi_1),$$

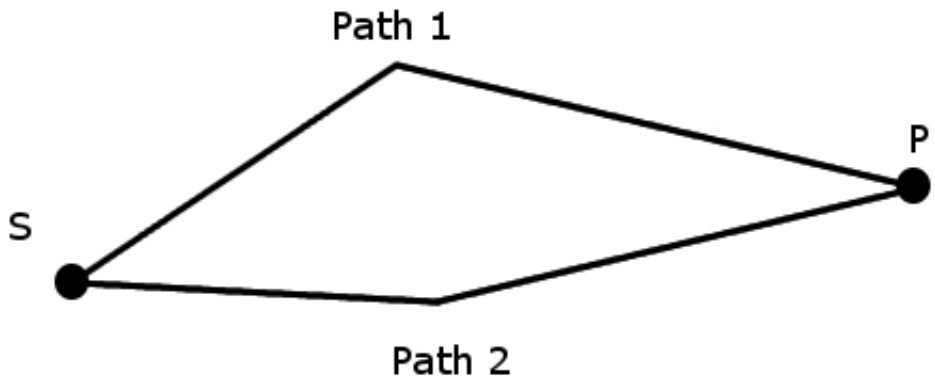

Figure 1.11: A ray diagram to illustrate the effects of path on patial coherence of the source. If path 1 is longer than path 2 by a distance greater than $v\tau$, where τ is the coherence time of the source, then there will be no interference at point P. However, if the path length difference is less than $v\tau$ then the rays will be partially coherent. The degree of partial coherence will depend on the degree to which the rays are in phase.

$$E_2 = A \exp i(k \cdot \mathbf{r} - \omega t + \phi_2),$$

The intensity of the combined waves is given by the modulus squared of E.

$$\begin{aligned} I^2 =& |E|^2 = (E_1 + E_2) \cdot (E_1^* + E_2^*) \\ =& |E_1|^2 + |E_2|^2 + 2Re(E_1 E_2), \end{aligned} \tag{1.10}$$

Suppose that E_1 and E_2 meet at a point P, far away, taking two separate paths (figure 1.11). One of these two paths will be longer by a time, τ. The irradiance at point P then becomes:

$$I^2 = |E_1(t)|^2 + |E_2(t+\tau)|^2 + 2Re(E_1(t)E_2(t+\tau)).$$

The interference term can be written more simply as:

$$2Re\Gamma_{12}(\tau),$$

where Γ is called the correlation function and is defined as

$$\Gamma_{ij} = (E_i(t)E_j(t+\tau)). \tag{1.11}$$

To define a normalized measure of the correlation function, the autocorrelation functions, Γ_{11} and Γ_{22}, are used . The degree of partial coherence is then:

$$\gamma_{12}(\tau) = \frac{\Gamma_{12}}{\sqrt{\Gamma_{11}\Gamma_{22}}}. \tag{1.12}$$

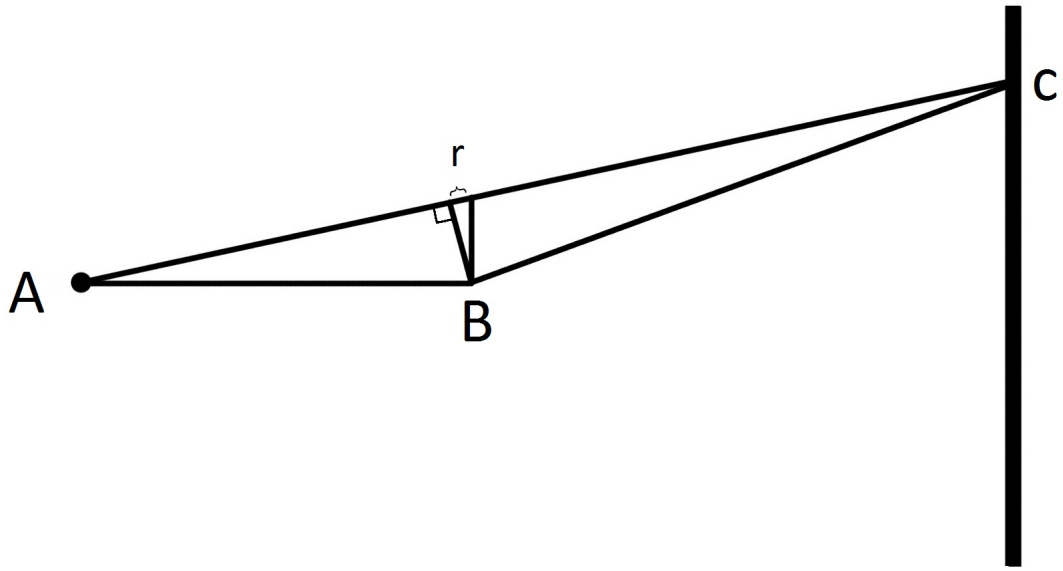

Figure 1.12: Schematic of reference and scattered waves interacting at a detector. If the coherence length is less than the path length difference, r, then the two rays are temporally incoherent. This will cause the hologram to be washed out, limiting the resolution.

By this definition, coherence can take three values. Complete coherence, $\gamma_{12}(\tau) = 1$, which will have the maximum contrast for fringes; partial coherence, $0 < \gamma_{12}(\tau) < 1$; and completely incoherent $\gamma_{12}(\tau) = 0$, which produces no fringes. [18]

There are two types of coherence: temporal and spatial[18].

Temporal coherence describes the length of time that a source emits a wave at a constant phase. Consider τ_0 to be the length of time that the wave train remains in phase. Random events such as collisions of electrons and neutrons in the solid state or source transformations limit the duration of τ_0 [18]. A source's coherence time is the time-averaged value of τ_0.

Figure 1.12 depicts a simple holography experiment. The two waves meet at the detector to create interference. The interference at point C on the detector can be seen as the interaction between paths AC and ABC. If path length difference, r, between ABC and AC is longer than the coherence legnth, then the waves will not interact to create a diffraction pattern. This causes a limit to the extent of the pattern, thus reducing the resolution of the hologram [18].

Another way to think of coherence time is by considering two overlapping waves with wave numbers k and k + dk. For a period of time, these two waves are in phase with one another. After a time, τ, these waves will destructively interfere, causing them to be incoherent (figure 1.13). A truly monochromatic source is a perfectly coherent source; lasers approximate this. This leads to the conclusion that the temporal coherence is related to the energy spread of the source[10]:

$$\tau = \frac{h}{\Delta E}. \tag{1.13}$$

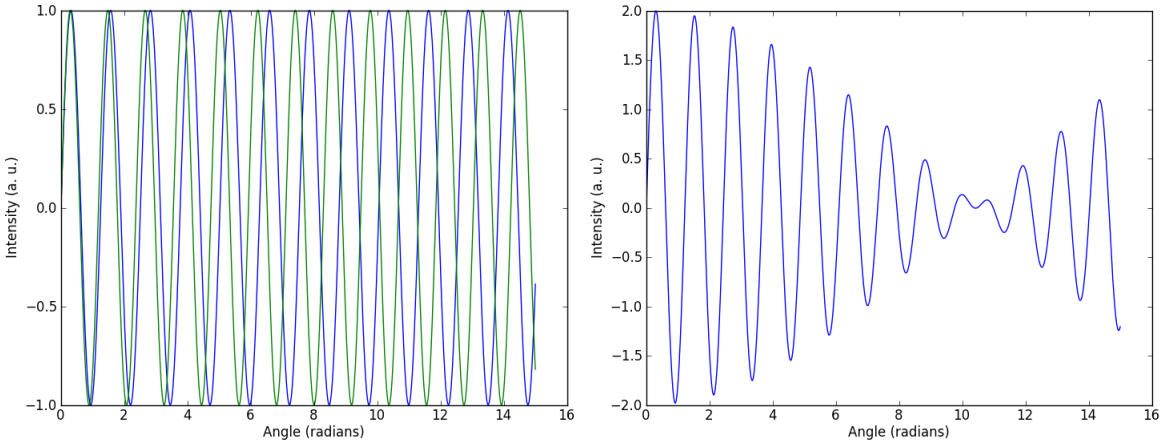

(a) (b)

Figure 1.13: a) Temporal coherence can be explained by considering two waveforms with wavenumber k and k + dk. Initially the waves are in phase but slowly decohere. The sum of the waves in b) shows a decay in the coherence due to the wavelength offset. The energy spread of the beam therefore limits the temporal coherence of the system.

A wavefront is defined by the "locus of points having the same phase" [19] such as a curve in 2D. Spatial coherence, for a spherical source, can then be defined as the degree to which the wavefront is spherically symmetric. This seems trivial; however, it is the limiting factor in electron holography. A perfect point source will emit a completely spatially coherent beam as it only emanates from a single point, creating a completely symmetric wave. Experimentally, all sources are extended sources, meaning that the electrons are being emitted from many different points. These overlapping spherically symmetric wavefronts will create a combined wavefront which reduces the spatial coherence of the source.

Consider Young's double slit experiment with two coherent sources, S_1 and S_2 (figure 1.14). Both sources create an interference pattern on the detector after interacting with the slits. For an individual source, the period of a pattern depends on the spacing of the slits, x, while the position of the central maximum depends on the position of the source. Therefore, the relative shift of the patterns is defined by the distance, d, between the sources. The shift in the patterns can also be seen as a shift in the phase of the sources. By placing the slits closer together, the period is reduced. Decreasing the period such that it becomes smaller than the phase difference in the sources, the fringes will overlap and be lost. This can be alleviated by moving the sources closer together to decrease the phase difference, which increases the transverse distance for which the total source is coherent. Therefore, an extended source has a lower transverse coherence length than a point source. Spatial coherence length can be defined by[10]:

$$L_t = \frac{\lambda}{(2\beta)^2}, \tag{1.14}$$

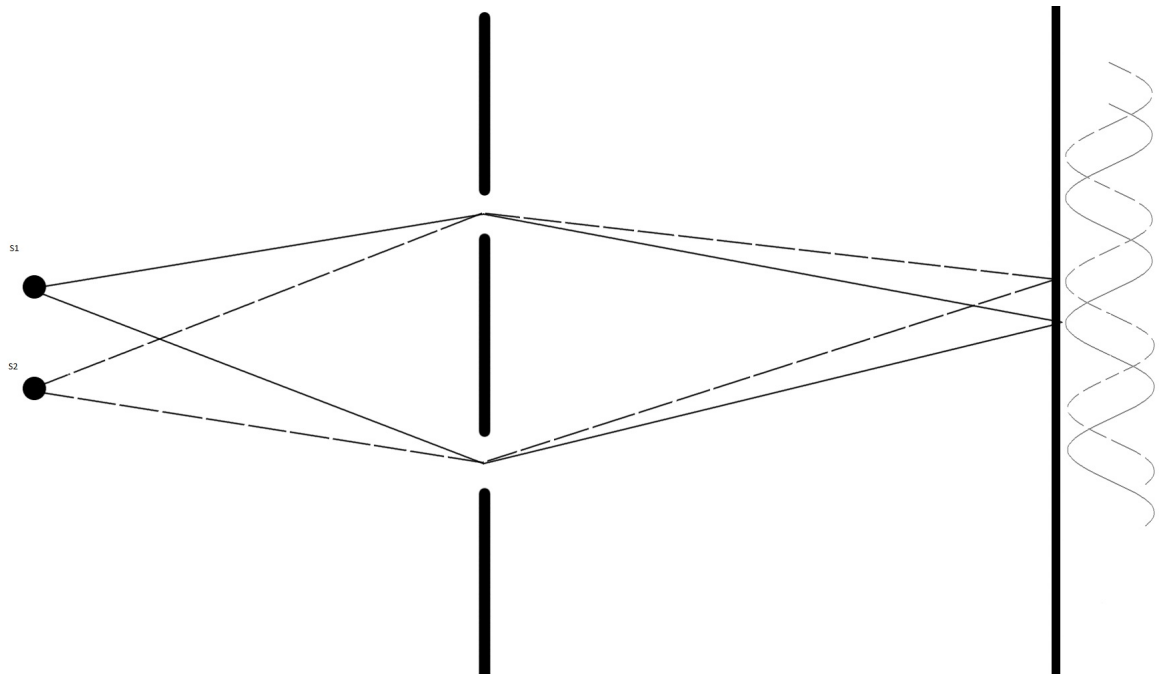

Figure 1.14: A double slit experiment with two sources. The separation of the slits defines the frequency of the individual interference patterns, while the distance between the sources defines the phase between the two patterns. The further apart the sources are, the more out of phase the patterns become, leading to shorter coherence lengths. By decreasing their spacing separation, the coherence of the source can be increased.

where β is the effective angular source size.

1.3 Previous experiments

Despite the small opening angle of his tips, Fink has observed some of the best holographic images to date. One of his most noteworthy works is a study of a DNA strand suspended using a TEM grid in a projection microscope. He obtained meaningful reconstructions of the DNA strands, showing no visible signs of degradation of the sample from the beam (figure **??**)[20]. This was corroborated in 2010 when Fink was able to show a strong correlation between images of biomolecules exposed for long periods of time. DNA strands were exposed to a beam of electrons at 60 eV for 70 minutes. Images were taken in 10 minute intervals and compared to the original. At 60 eV, and for energies below 260 eV, the images remain more than 90% correlated, leading to the conclusion that there is very little sample damage from the beam[21].

In 2009 Stevens performed a theoretical experiment on how the opening angle of the source would affect holography. In this study Stevens simulated holograms of DNA with sources with different opening angles. He was able to show that in order to obtain a large NA for the microscope, a large opening angle of the beam is necessary since a hologram

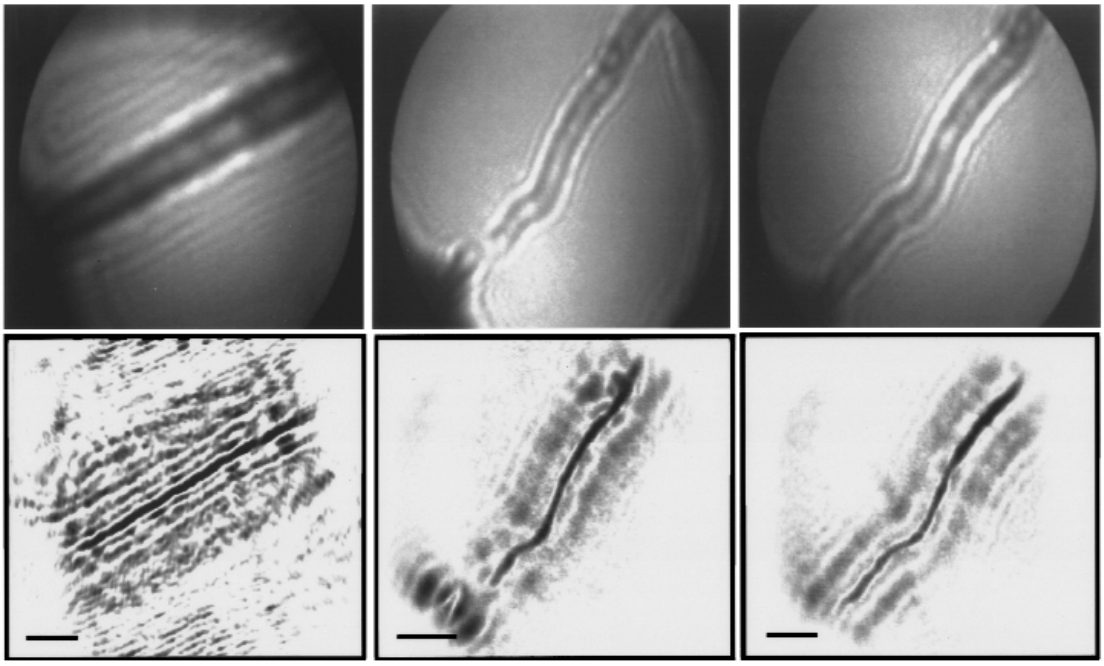

Fig. 5. DNA holograms and reconstructions. Left, 50 eV, bar 20 nm; center and right, 70 eV, bar 40 nm.

Figure 1.15: Work performed by Fink on damaged caused by low energy electrons on DNA strands. The top three images are holograms of a DNA strand while the bottom three show their reconstructions. The energy of the reference beam is, from left to right, 50 eV, 70 eV and 70 eV. [20].

can be no wider than the width of the reference beam. To obtain large opening angles, tips with high aspect ratios are needed. Figure 1.16 shows the effect of NA on beam divergence and the resulting holograms[22].

Until recently, holography studies have been limited to filamentous samples, which can span across a gap on the order of a micron. The issue is that low energy electrons have short attenuation lengths. No material available was thin and robust enough to hold a sample to act as a microscope slide. Mutus et al. pioneered the use of graphene as a supporting substrate. Graphene has been shown to be 97% transparent to electrons at 100eV and is strong enough to support samples[23]. This opens the field to new, previously untested, samples.

1.4 Going further

Electron holography, though it has been in development for 60 years, is still a young technique. As such, there are many aspects that still need to be standardized and improved upon. Low energy electron holography provides a way to obtain the structure of fragile objects without the need to average over a large number of samples.

In order to suspend samples, graphene needs to be placed on TEM grids. Currently,

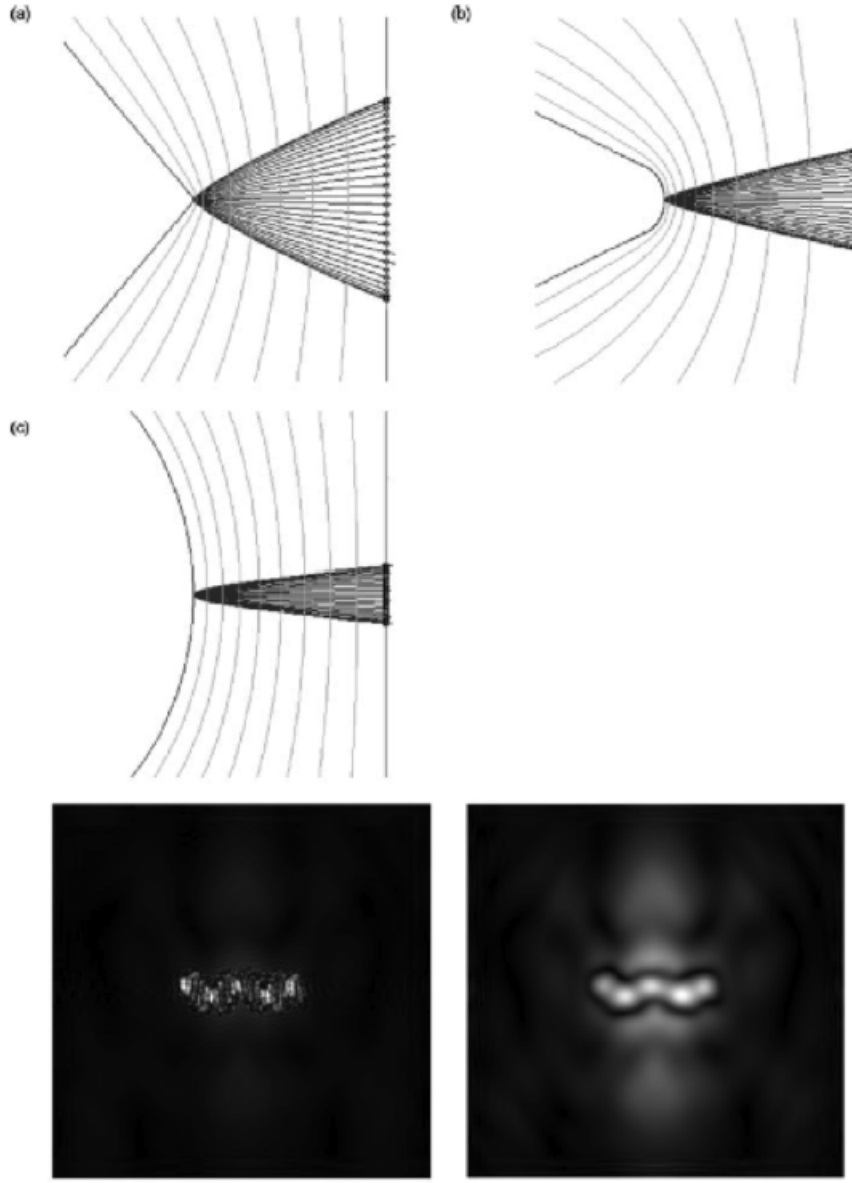

Figure 1.16: Work performed by Stevens on the effects of tip shape on the opening angle of a source. The study showed that higher aspect ratios lead to more divergent beams seen in a)-c). Image d) and e) show reconstructions of simulated DNA strands from high and low aspect ratio tips, respectively. Finer details of the DNA strand are present in d) due to the high aspect ratio of the tip. [22]

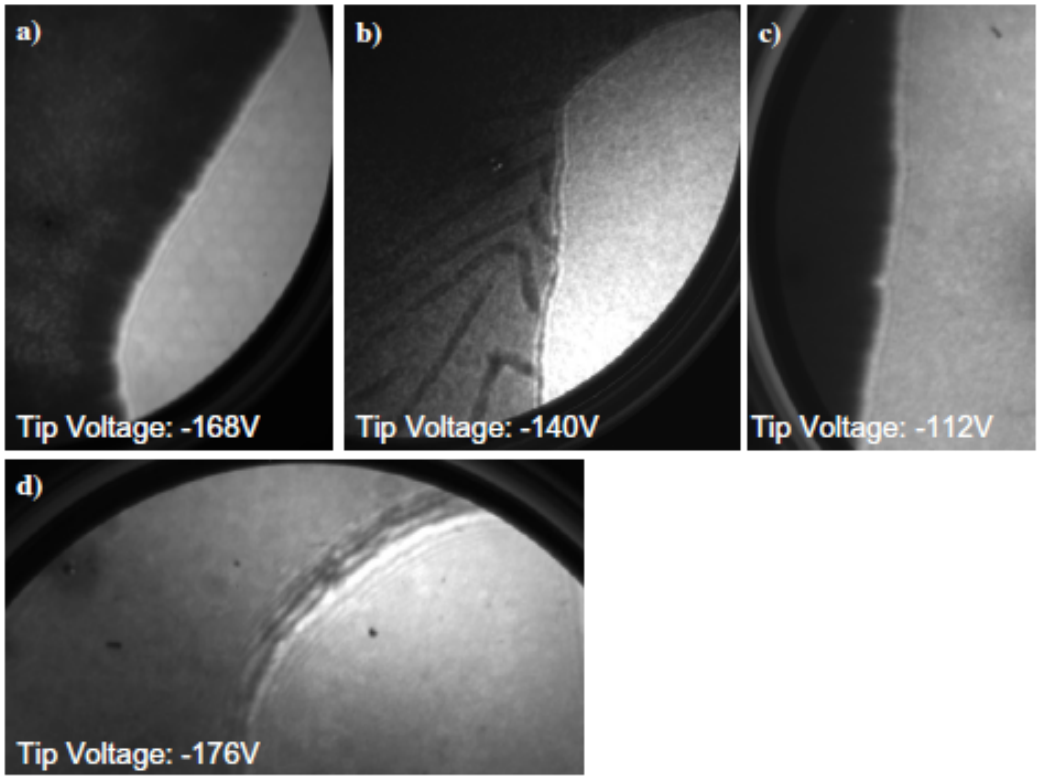

Figure 1.17: Work performed by Mutus on resistive heating of graphene on TEM grids. A graphene sample in ultra high vacuum shows an opaque edge due to contaminants on the surface. The sample is very sensitive to heating temperature and duration. Images a) through d) show the effects of prolonged heating of the graphene. a) 300°C for 40 min, b) 420°C for 90 min, c) 300°C for 90 min, d) 400°C for 8h.[23]

there are no companies which provide graphene on TEM grids. Chapter 2 will discuss the growth of graphene and its transfer onto arbitrary substrates.

Chapter 3 will cover methods required to prepare for and operate the PPM.

Chapter 4 covers the methods of observing, storing and analyzing data using a Labview program developed in house. The program improves on signal processing and analytical methods used previously. A discussion of current trends in electron holography will also be discussed in detail.

Chapter 2

Growth, Characterization and Transfer of Graphene

Over the last decade, graphene has become one of the most heavily studied materials in the world. Graphene is a honeycomb sp^2 bonded lattice with a bond length of 1.42 Å. Stacked graphene (graphite) has an interlayer spacing of 3.35 Å.[24] The material attracts a lot of attention due to its many amazing parameters such as its optical transparency, conductivity and elasticity,[25] to name a few. The exceptional material properties make it ideal for many applications such as flexible electronics and photonics.[25]

One potential application is field-effect transistors, the most basic structure in CMOS electronics. The high conductivity of the film allows for extemely high switching frequencies[26], which would be ideal for communications-related applications[27]. The development of high frequency transistors is limited by the absence of a bandgap in high quality graphene[25]. Thus, the transistors cannot be fully turned off. Solutions to the bandgap problem, such as graphene nanoribbons[28], bilayer graphene[29], and controlled damage to the graphene layer [30], are currently being studied. Graphene transistors have also shown that they do not exhibit a temperature dependence[31], making them ideal for low temperature systems.

Graphene is not limited to applications in the field of electronics. Many studies have shown that graphene is impermeable to gases, including helium[32]. Graphene can provide a method of protecting samples from oxidization or evaporation during transport. The material can also provide a means of eliminating helium leaks in vacuum applications. Graphene can also be used as a filter for desalination by means of reverse osmosis[33], which would provide potable water in regions where fresh water is scarce. Another promising area of research on graphene is its application to transparent conductive electrodes.

Touch interfacing with devices is becoming one of the most common ways to interact with technology today. Touch screens are employed in many disciplines and in daily life through superphones. Graphene's high optical transparency and conductivity make it a candidate for touch screens and other transparent electronics. The most common conducting transparent electrode today is indium tin oxide. The material is expensive and is becoming more rare, pushing prices higher[25]. Graphene, which can be mass produced at low costs, is far more

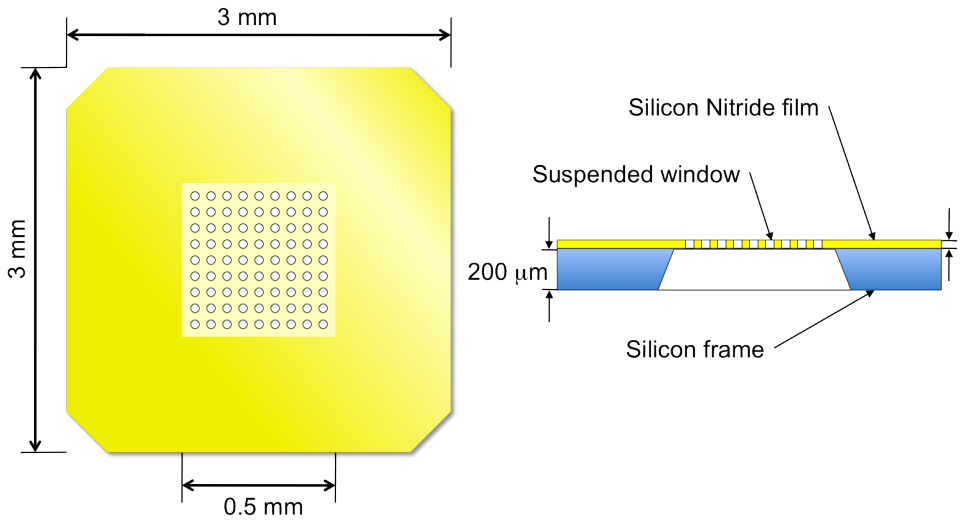

Figure 2.1: Schematic of a gold coated TEM grid used in holography experiments. The silicon nitride window is used such that electrons can pass through unattenuated. The thickness of the membrane is 50 nm while the dimensions of the window are 0.5 mm by 0.5mm. Reproduced from [11]

economical. Graphene's transparency is not limited to the visual spectrum. Graphene remains transparent to electrons in the range of 60 - 200 eV. This, coupled with graphene's strength, makes it the ideal microscope slide for electron holography.[23] Graphene makes it possible for holography to image non-filamentous samples on a silicion nitride grid.

A silicon nitride grid is a freestanding array of holes on a very thin (50 nm) silicon nitride membrane (figure 2.1). The membrane is grown on top of a 200 μm thick silicon wafer support. The center of the silicon wafer is back-etched until only the membrane remains. The membrane is perforated such that there are 2 μm diameter holes at a 4 μm pitch. The nitride grid is coated with gold such that it is conducting. The grid, without graphene, requires that the samples must span across the diameter to be supported. Graphene allows for samples to be placed anywhere within the pore. The thin film also provides an equipotential plane for incoming electrons.

The path of electrons from the source depends on the local field within the microscope. Fields in the direction perpendicular to the motion of the electron can cause the trajectory to curve, which leads to great distortions in holography. An example of this effect can be shown in a PPM study of carbon nanotubes (CNT). The presence of the negative tip causes a positive charging effect on the CNT.[34, 35] The CNT acts as a bi-prism, which creates curved equipotential planes (figure 2.2a), leading to non-linear electron paths. Graphene placed on the grid creates flat equipotential planes (figure 2.2b), which would eliminate potential convolutions. [23]

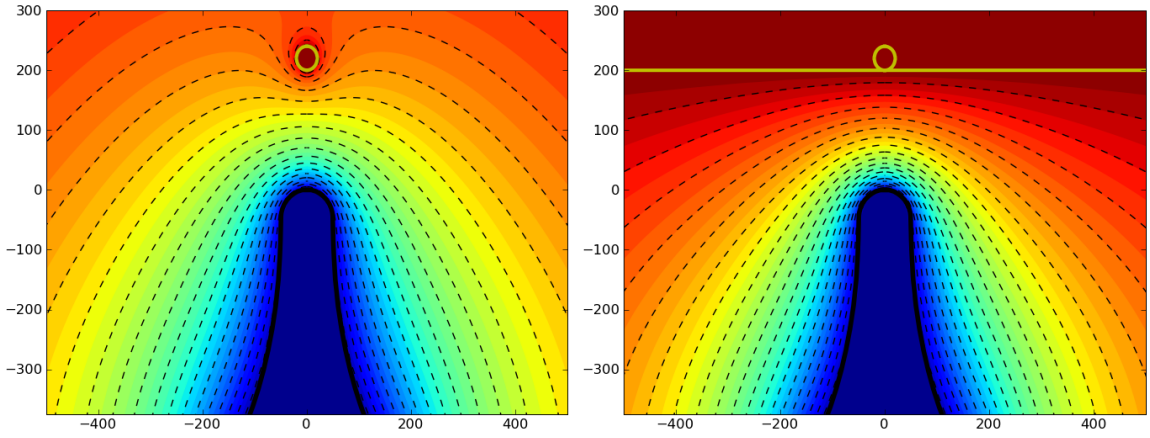

Figure 2.2: A suspended CNT creates curved equipotential planes in a) which results in electron trajectories being curved making reconstructions more difficult. b) Placing graphene down behind the CNT creates flat equipotential planes, removing the convolution. Reproduced from [23].

2.1 Obtaining Graphene

The first attempts to isolate single layer graphite, in the 1960s, used a process called intercalation, which inserts atoms between layers of highly oriented pyrolytic graphite (HOPG). The separated layers were identified using electron energy loss spectroscopy (EELs), which showed a "softening" of bonds between the surface layer and the bulk.[36, 37, 38] In 2004 a more robust method was invented by Andre Geim which led him to win the Nobel Prize in 2010. [39]

The Scotch Tape Method was the first method which allowed graphene to be transferred to arbitrary substrates. Isolation is then achieved by sticking a piece of tape to the HOPG to remove many layers of graphite. A single layer is obtained by sticking the graphite layers repeatedly onto new pieces of tape. The tape is placed in an acetone solution where it dissolves, and the graphene is sedimented onto a silicon oxide wafer for observation [40]. The Scotch Tape method creates the highest quality graphene known to date, though the process is not scalable for semiconductor applications.

The most likely candidate for isolating CMOS-ready graphene sheets is a process which uses silicon carbide (SiC). SiC is a material which is currently used in the semiconductor industry for high temperature transistors and LEDs. Sheets of any size can be prepared by heating a SiC wafer to >1100°C. The heating causes silicon to selectively sublimate from the surface, leaving the carbon behind. The remaining carbon bonds together to create large sheets of graphene. [41, 42] The tools used to prepare SiC can also be used in conjuction with graphene, which makes this method of growth very powerful for the semiconductor industry. The graphene grown using SiC does not provide the same high

conductivity as that obtained via the Scotch Tape Method, nor is it as easily transferrable to other substrates.[25]

More recently, graphene has been isolated using a process called low pressure chemical vapor deposition (LPCVD). Graphene can be grown by subjecting a catalyst to an appropriate ratio of hydrogen and a carbon source, such as methane, in a high temperature environment.[43, 44] Many different catalysts exist, including nickel, ruthenium and copper.[45] Most LPCVD graphene is grown on copper because copper has low carbon solubility[46], which allows for reliable growth of monolayer graphene. During growth, high temperatures will allow carbon to diffuse into the catalyst, which will settle out while cooling to create multilayer graphene. Copper also allows for large graphene crystals due to the small lattice mismatch, which leads to better electronic properties.

The process for growing graphene is as follows. To prepare the samples, 2 cm squares of copper with 25 μm thickness (from the company Alfa Aesar) are cut from the roll. Due to the packing methods, the copper sheets have a bulk curvature which can be removed using a rolling pin. The copper is dipped in acetone for 10 s to remove organic contaminants, followed by a rinse in deionized (DI) water. The copper is then subjected to an acetic acid bath of 5 percent concentration for 10 minutes. The purpose of the acid is to remove any oxide which may have formed on the copper surface. The copper is then rinsed in DI water, dipped in acetone and then isopropanol to remove any acetone organics. The rinsing and dipping steps take 10 seconds each. To differentiate between the front and back of the sample, a corner is folded onto itself to indicate the upward direction. This is a necessary step since graphene will grow on any exposed copper.

Once the samples are ready they are placed in the system seen in figure 2.3. The system consists of a clamshell tube furnace, precursor gasses hydrogen and methane, and leak lines. The gas cylinders are connected to the furnace chamber using 1/4" stainless steel tubing. To control the flow of gasses, two swagelok leak valves are placed in series (figure **??**). The quartz tube, which has a 1.1" outer diameter and 0.9" inner diameter, is sealed using a KF25 to 1 1/8" Quik-Disconnect port from MDC. The system is pumped down using an Edwards RV3 rotary pump which uses Fomblin oil. This oil is needed because the gases being pumped are flammable and explosive. The pump is attached directly to the leak lines in order to facilitate faster cleaning of the lines through the use of a Swagelok valve. A molecular sieve trap is used to ensure that the system does not experience any backstreaming.

The samples are placed on a quartz slide which is used to keep the samples flat during growth. The slide is loaded into the centre of the furnace tube using a long aluminum rod. The system is then sealed and pumped down below 30 mTorr. The lid of the furnace is closed, hydrogen valve is opened and the hydrogen flows to achieve a partial pressure of 200 mTorr. Sudden changes in pressure can cause the samples to be blown off the slide, which requires the use of caution when increasing the flow of gasses. To grow graphene, the

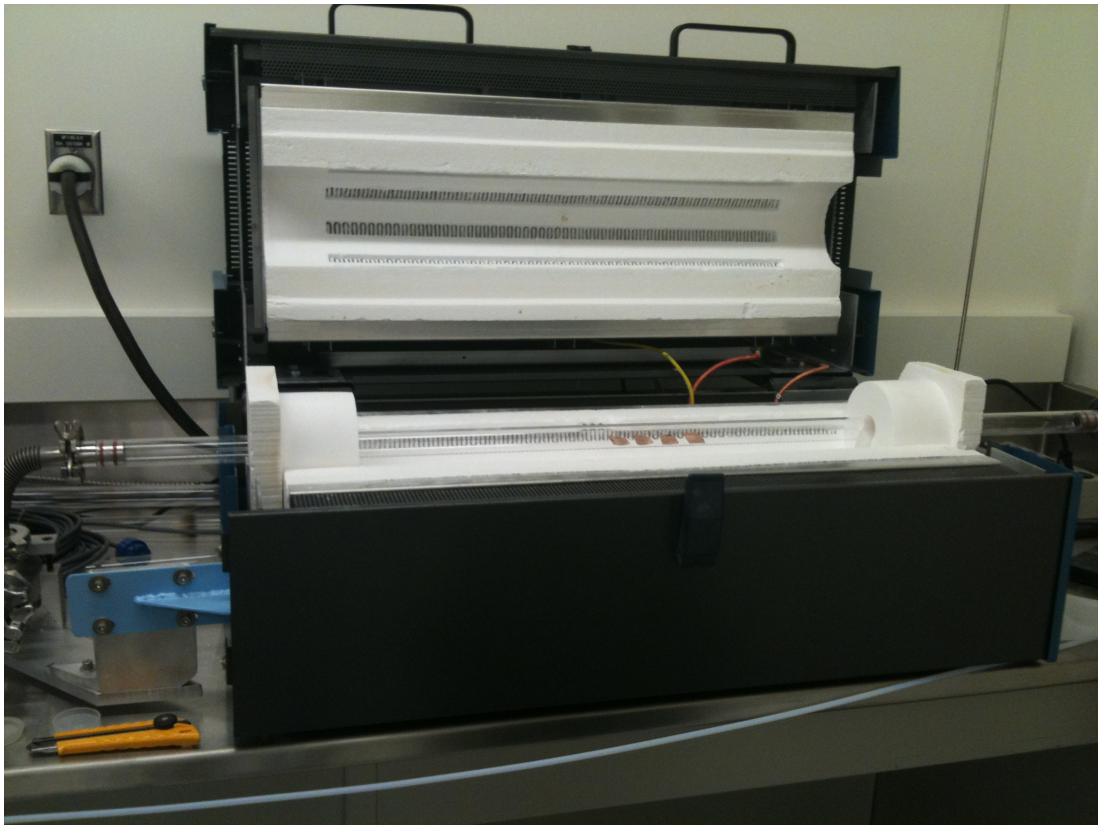

Figure 2.3: Clamshell furnace used in graphene growth. The clean copper samples are loaded into the quartz tube and pumped down to 30 mTorr before leaking in hydrogen and heating the system to 1000°C.

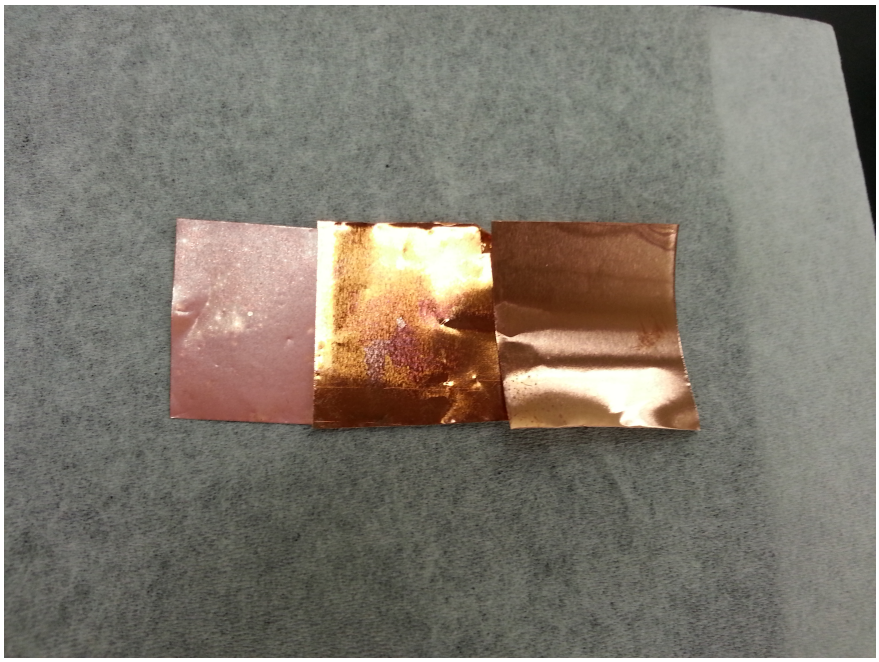

Figure 2.4: Examples of copper samples grown in our system. From left to right: Oxidized copper, graphene on copper, and clean copper.

substrate must reach a temperature of 1000°C. With hydrogen flowing, the temperature is slowly ramped up to the desired level. Once the system is at 1000°C, the copper is allowed to anneal for 10 minutes. The purpose of the annealing is to allow the copper surfaces to reorder themselves to yield larger single crystal regions.[44] Once the annealing is complete, the methane valve is opened to achieve a partial pressure of 14 Torr and graphene is allowed to grow for 20 minutes. When growth is complete, the furnace is turned off and opened to quickly quench the samples. Rapid cooling is used to limit the amount of carbon which will diffuse out of the copper substrate to create multilayer graphene. Once the furnace has reached 150°C, the leak lines are closed and the pump is turned off. To bring the system up to atmospheric pressure, the argon valve is opened, such that samples can be removed.

Initially, the growing apparatus used mass flow controllers to leak gasses into the system. Though said to be leak-tight, the samples in the system were being oxidized, which resulted in failed growths. Successful trials began once the flow controllers were replaced by leak valves. Partial pressures became the method of controlling growth. The success of the growth was gauged visually; if the copper samples looked like anything that was not copper, then the growth had failed and the copper had likely oxidized. The copper samples, when coated in graphene, tended to have a more qualitatively reflective surface than the clean copper samples. Figure 2.4 shows an oxidized copper sample, copper with a graphene sample and a clean copper sample. The visual test is followed up by a more robust inspection using different techniques.

2.2 Characterization

At first, graphene was most commonly identified using atomic force microscopy (AFM) by measuring the topology of the surface. Early on in graphene's lifetime, the thickness indicated by AFM, $1nm$, was much larger than expected for single layer graphene, causing experimentalists to assume more than one layer was present. [24] Geim discovered graphene in 2004; he accompanied the discovery with a new method of identifying the material.

Raman spectroscopy is a surface sensitive technique that uses laser light, of known wavelength, to probe phonons in a material. Raman spectroscopy has become one of the main methods for characterizing graphene, due to its simplicity. The light interacts with the phonons via inelastic scattering to create an excitation. The spectrometer measures the change in energy of the outgoing radiation. Raman was first used on carbonaceous materials in 1973 by M. Nakamizo et al. In their paper they identify Raman peaks for HOPG at 1350 cm^{-1} for the D peak and 1580 cm^{-1} for the G peak. Later studies of HOPG show a further peak, the 2D peak, at 2700 cm^1.[47] Recent studies show that the position of the peaks is similar for graphene. The difference between graphene and graphite is the relative intensity between the G and 2D peaks. While graphite has a larger intensity at 1580 cm^{-1}, graphene has a more intense peak at 2700cm^{-1}. [48]

Not only can Raman spectroscopy identify the difference between graphite and graphene, it can also differentiate between single layer, dual layer and multilayer graphene by using the full width at half max (FWHM) of the 2D peak and a ratio of the 2D with respect to the G peak. The 2D peak of single layer graphene is located at 2682cm^{-1}, and has a ratio of 4:1 with a FWHM of 32 cm^{-1}. [48] Figure 2.5 shows the typical spectrum for a single layer of graphene on an SiO_2 substrate. Raman spectroscopy is unable to identify whether the sheet of graphene is continuous because of its large spot size, which is on the order of a micron.

Characterization was first performed on copper to ensure that graphene was indeed present. Identifying the number of layers of graphene on copper is not possible due to copper's strong background in Raman spectroscopy. Figure 2.6 shows a typical 10 spectral acquisition of 20s duration with a 4 mW power from a 514 nm laser. Both the G and 2D peak are present in the figure. The ratio of the two peaks is approximately 4:1, which identifies the sample as graphene. However, due to the position of the peak and the width, it is not possible to identify the number of layers.

Further investigation of graphene on copper can be done in an ultra high vacuum. Figure 2.7 shows a typical sample holder for the system used in this study. Due to the thickness of the copper foils, the sample holders are unable to make proper connection to the surface. As such, the sample holder had to be modified to load the samples. A silicon wafer 3 mm by 12 mm was placed beneath the copper foil as a support. To make contact with the clips, two small pieces of silicon were placed between the clips and the copper foil to allow for resistive heating (figure 2.8). Once the sample was loaded it needed to be cleaned. The

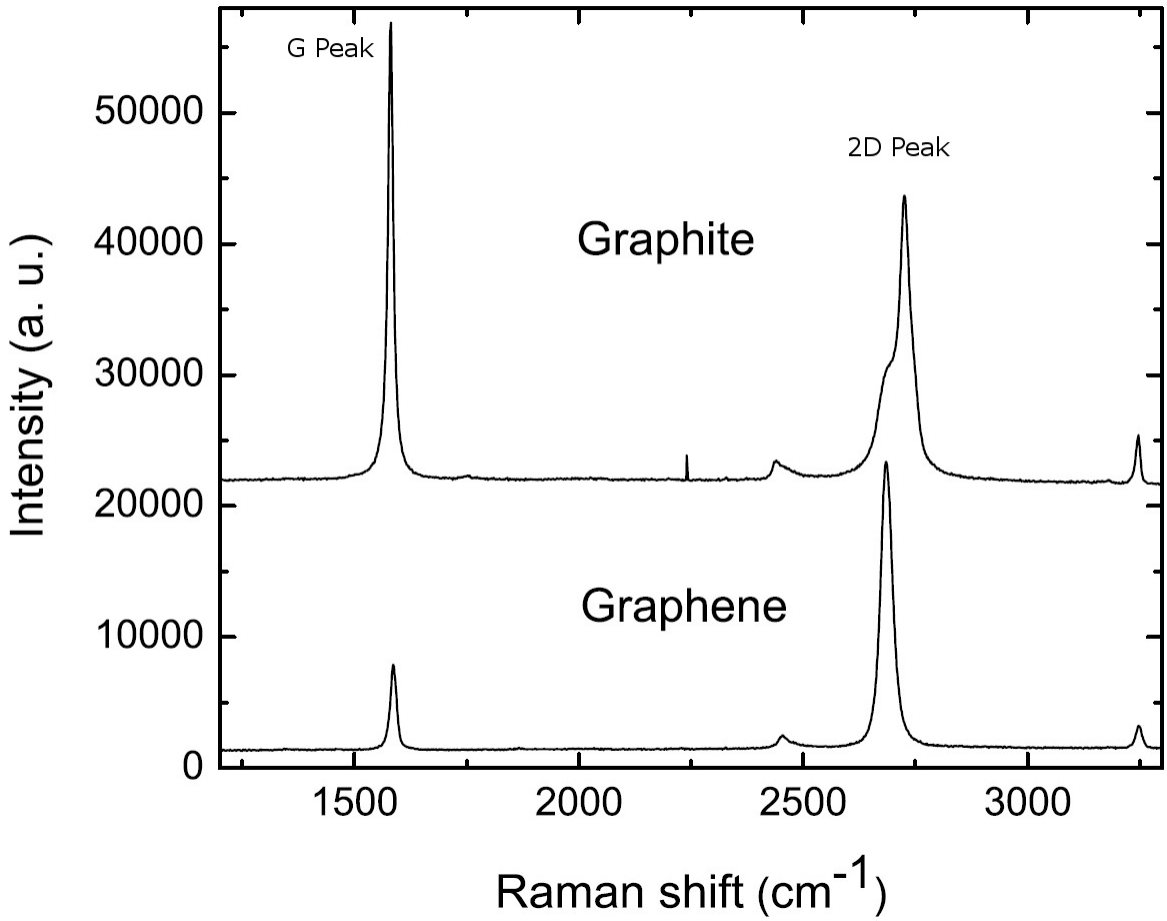

Figure 2.5: A typical Raman spectra of monolayer graphene on SiO_2 using a 514 nm laser. Here the G and 2D peaks characteristic of graphene appear. The difference between graphene and graphite is the ratio of the peaks. Graphite has a 1:2 2D to G while graphene has a 4:1 ratio. Reproduced from [48].

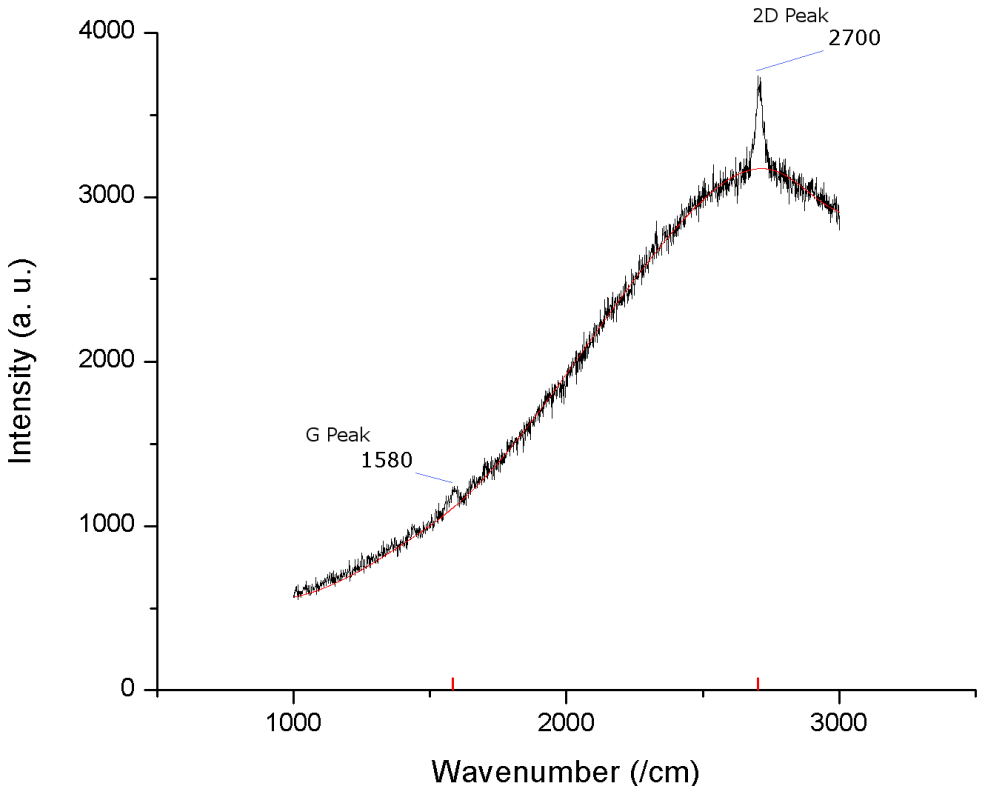

Figure 2.6: A raman spectrum obtained of graphene on copper. The background of copper and the shift in the second peak make it impossible the number of layers of graphene. The red line represents the baseline of the copper background. The fit was obtained by using a high order polynomial (16). The cause of the background is unknown, though it is assumed to be the copper substrate since it is not present in transferred samples.

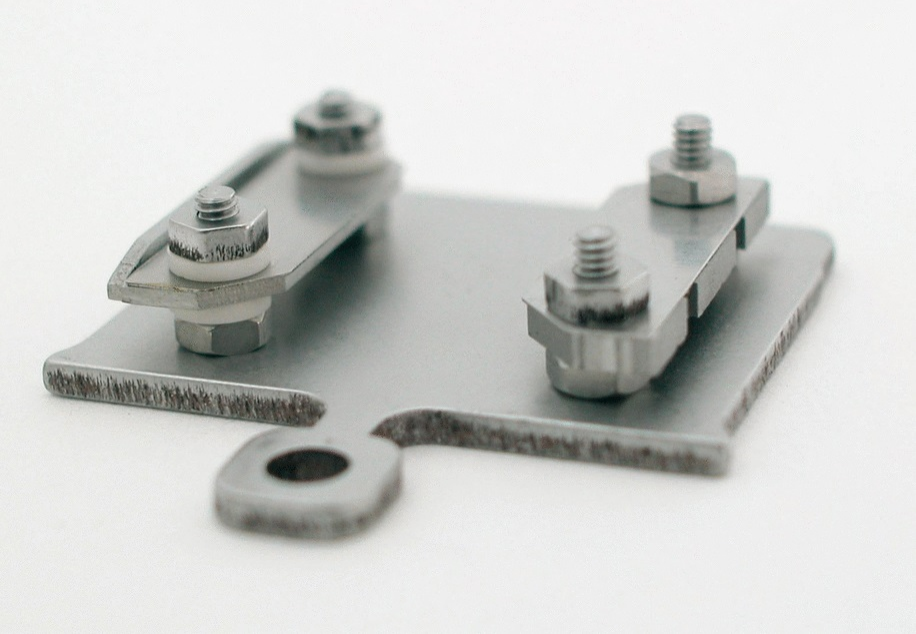

Figure 2.7: Typical sample holder used in the Omicron STM1 microscope. Reproduced from Omicron website.

sample was heated using a direct current up to 300°C for two hours.

High resolution EELs (HREELs), a method similar to Raman in that it detects the loss of energy of an initial beam, could be used to probe plasmon modes or higher order effects in phonon modes based on defects in the graphene. The idea was to compare Raman spectra to HREELs spectra in hopes of seeing more information about the thin film. Initial HREELs measurements of graphene on copper used an accelerating voltage of 3.2 eV. No Raman active modes – namely the D, G, and the 2D peaks – were seen in this study. In 2001 Ryder et al. showed that the G peak can be seen in specular reflection using an accelerating voltage of 17.6 eV.[49] The study was performed on in-situ grown graphene on nickel. The specular spectra showed a distinct peak at 1580cm^{-1}.

Figure 2.8: Schematic of the alterations required to mount a graphene on copper foil sample in the STM1. The SiO_2 wafer serves as a substrate support. The silicon between the graphene and the sample holder clip is used to facilitate resistive heating.

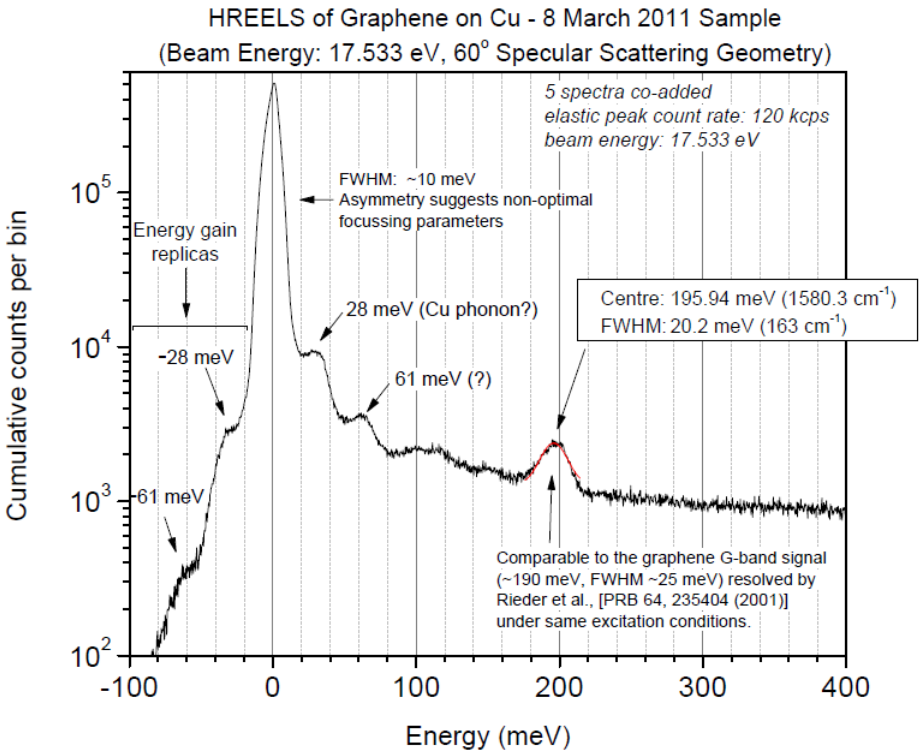

Figure 2.9: HREELs spectrum of graphene on copper taken with a beam energy of 17.6 eV on-specular 60°. The only feature from graphene is the 1580 cm^{-1}, or G, peak while the 2D peak does not appear.

The experiment was replicated on the in-house CVD graphene to yield similar results (figure 2.9). The spectrum shows a distinct peak at 1580 cm^{-1}. However, as in Ryder et al., the 2700 cm^{-1} peak is missing. The spectrum also has an assymetric peak due to the high accelerating voltage, which reduces the resolution of the measurement. Further conclusions would require a more in-depth study, including a full off-specular treament.

Scanning tunneling microscopy (STM) could provide a method for measuring the size of a graphene domain and the graphene's overall defect concentration. Measurements of graphene on copper in an ultra high vacuum (UHV) environment proved to be successful in a handful of trials. Imaging parameters for the study were 2V bias with a 100pA current. Though the distinct character and bond length could be seen (figure 2.10), the sample was dominated by large corrugations. The presence of the corrugation was reproduced in an STM study of freestanding graphene. The resulting images show a similar morphology of the surface. [50] This leads to the possible conclusion that these areas are indeed due to corrugations of the substrate. However, this would be a hasty conclusion due to the fact that the sample substrates are very different. The lack of clarity could also be due to the limited cleaning during preparation. The lack of clarity could be due to graphene not being present in these regions and only the coarser scale copper could be seen. There is also a

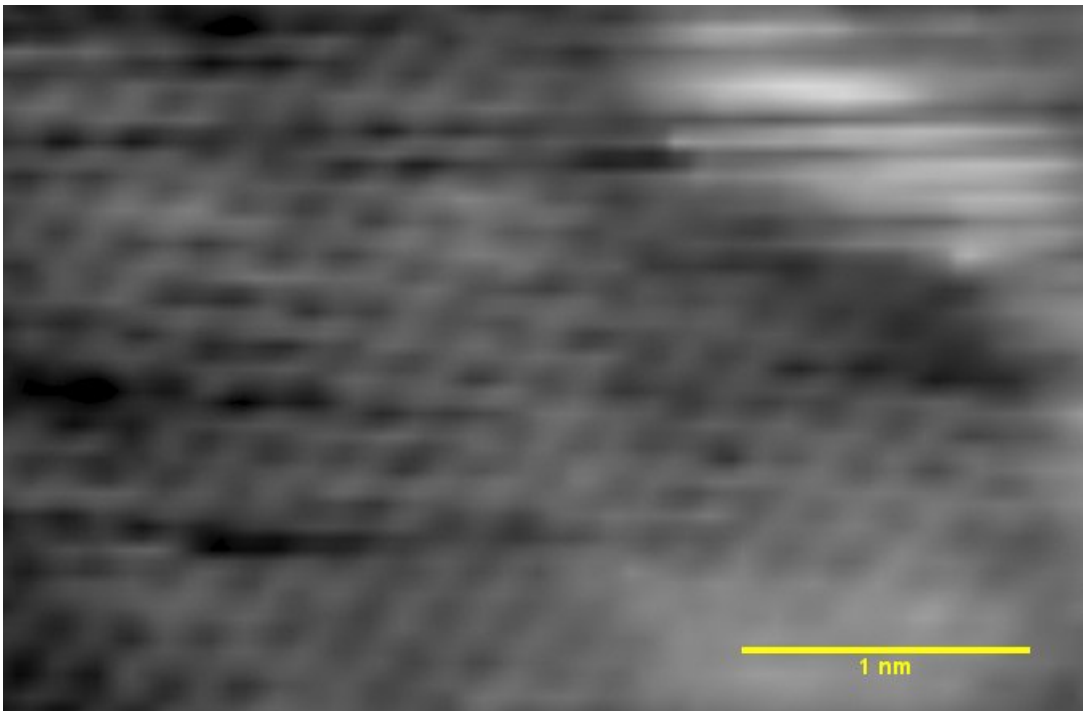

Figure 2.10: STM of a graphene on copper sample. The characteristic bond length, 1.42 Å, of graphene can be seen. However, there is a macro fuzziness or corrugation caused by the underlying copper substrate.

small chance that the imaging conditions were not optimal for imaging graphene on copper. As such, the electrons could have been tunneling directly into the bulk copper. Similar studies performed on a graphene copper sample show beautiful images.[51] However, those samples were grown at very low pressures, which reduces the presence of contaminants. Learning more about the graphene surface requires a transfer to SiO_2.

Another method of identifying graphene is to identify the film using white light. Graphene on a SiO_2 substrate can be easily identified by its light blue colour. Graphene becomes visible due to constructive interference between the reflected light from the graphene-to-oxide interface and the oxide-to-silicon interface.[52] The methods described above are able to confirm the presence of graphene. However, they are unable to identify the continuity of the sheet.

2.3 Transferring Graphene

Once graphene has been grown and identified, it needs to be transferred to a grid for holography. There are many approaches to transferring graphene. Below, a "standard" transfer and a "direct" transfer will be outlined.

A standard transfer begins by cutting the 2 cm by 2 cm sheets of copper into 3 mm by 3 mm squares such that their size is comparable to a grid. The sheets are spin-coated with

PMMA 495 A2 at 2000 RPM for a minute and allowed to dry at 85°C for 5 minutes. Once dry, the sample is placed PMMA-side up in a 3 M solution of ammonia persulfate to etch the copper. Lower concentrations of the etchant will suffice; however, they will increase the etch time. To ensure quick etching, it is suggested that the backside of the copper first be exposed to an oxygen plasma in order to remove graphene from the bottom of the foil. Once the copper is fully etched, a small, thin film of PMMA will be visible floating on the top of the etchant. The sample will be floating with PMMA-side up, assuming there have been no major perturbations to the etchant. Using a clean silicon wafer and a pair of plastic tweezers, scoop up the film and place it in a DI water bath for 24 hours to remove any lingering etchant. Using the same method, scoop the PMMA thin film onto the TEM grid. Heat the grid at 150°C for 20 minutes to promote adhesion between the grid and the graphene. Submerge the sample in an acetone bath for 60 seconds to remove the PMMA. Rinse the sample in isopropanol to remove the acetone. PMMA can also be burned off the surface in a 50% hydrogen atmosphere at 300°C.[53] Both processes leave residual PMMA on the surface.

Many attempts were made to use the standard technique. Most ended in failure. The issue with the transfer was that once on the SiO_2, the graphene became disconnected, resulting in small clusters of graphene "islands" of graphene (figure 2.11). Initially, ferric chloride was used as the etchant, which resulted in the substrate dying. Raman was used to characterize the samples, which showed sporadic coverage of the surface. This shows that graphene has been transferred, but not well. More recent attempts to transfer graphene, using ammonium persulfate to etch copper, have been more successful. Figure 2.12 shows a surface plot of multiple Raman spectra along a given line on a grid. Though the sample looks bare, the Raman line spectrum shows that it is covered in graphene.

The direct transfer method uses no intermediate substrate, which in theory limits the number of contaminants present on the graphene. The method was developed previously by Zettl et al. (figure 2.13). Once the graphene has been grown, the copper sample is placed face-up on a clean surface. The TEM grid is placed face down on top of the graphene, such that the nitride membrane is in contact with the graphene surface. A droplet of IPA is put on the TEM grid such that the process of evaporation brings the two surfaces closer together using surface tension. Once completely evaporated, the copper and grid are floated in the etchant, copper-side down.[54] This allows the graphene to be transferred without ever placing PMMA on the sample, which would eliminate both the PMMA and acetone residues.

The results for the direct method are not very promising. The continuity of the sample is very poor and the surface was dyed by the ferric chloride used in early attempts. Figure 2.14 shows an image of the transfer. The colourful areas are the regions where graphene is present, whereas the rest shows weak Raman signals.

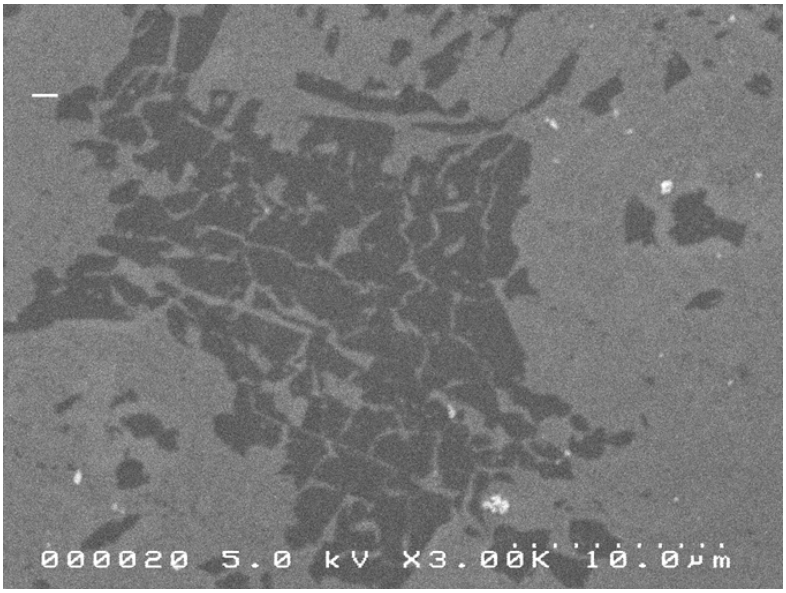

Figure 2.11: Scanning electron microscopy image of initial attempts at transferring graphene onto SiO_2 at 5.0 kV. The dark regions are graphene covered while the lighter regions are the SiO_2. The coverage is seen to be disconnected making the transfer of insufficient quality for electron holography applications.

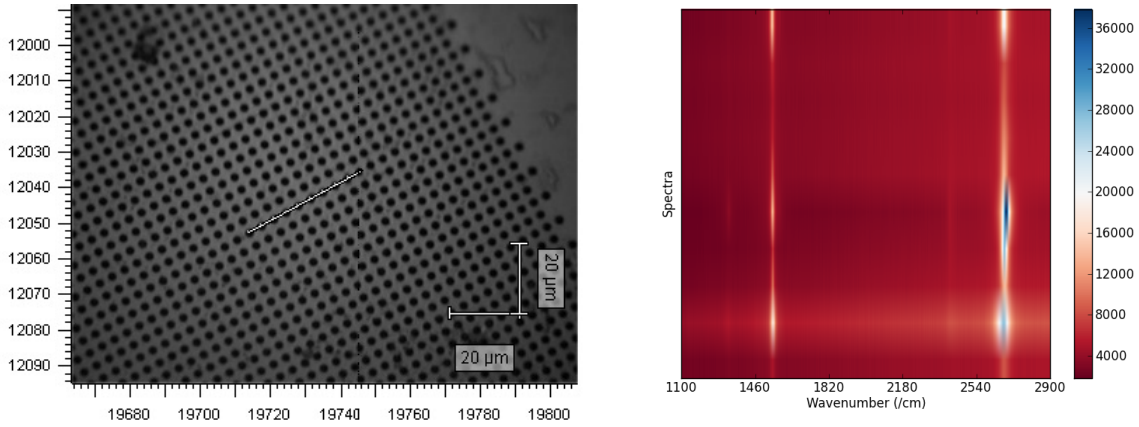

Figure 2.12: Raman line spectra of recently grown graphene transferred to TEM grid. a) shows the positions of the individual spectra. b) shows the intensity of the 1580, G, and 2700, 2D, peaks. The position and relative intensities show that this sample is covered in graphene in the region of the pores.

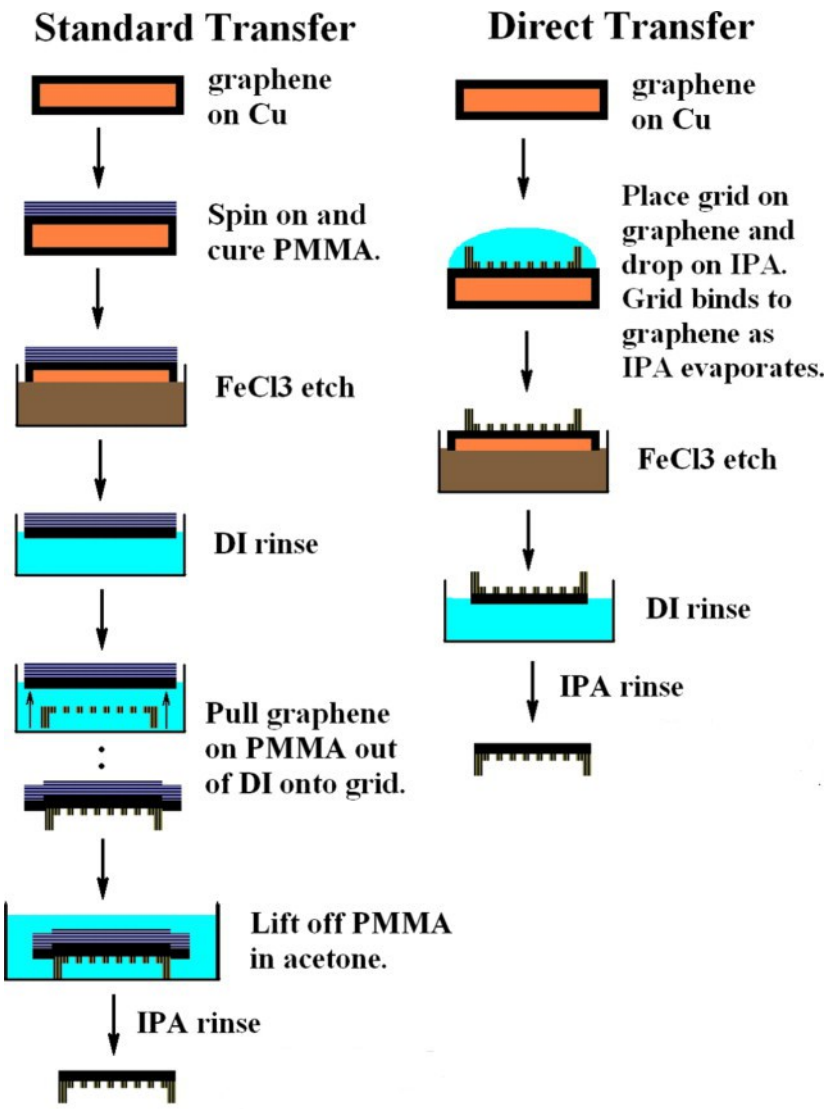

Figure 2.13: Work done by Regan et al. The standard process (left) is typically used but leaves a PMMA residue on the graphene. The process for the direct transfer of graphene is outlined on the right. The direct transfer of graphene to a TEM grid would greatly reduce the contaminants on graphene.

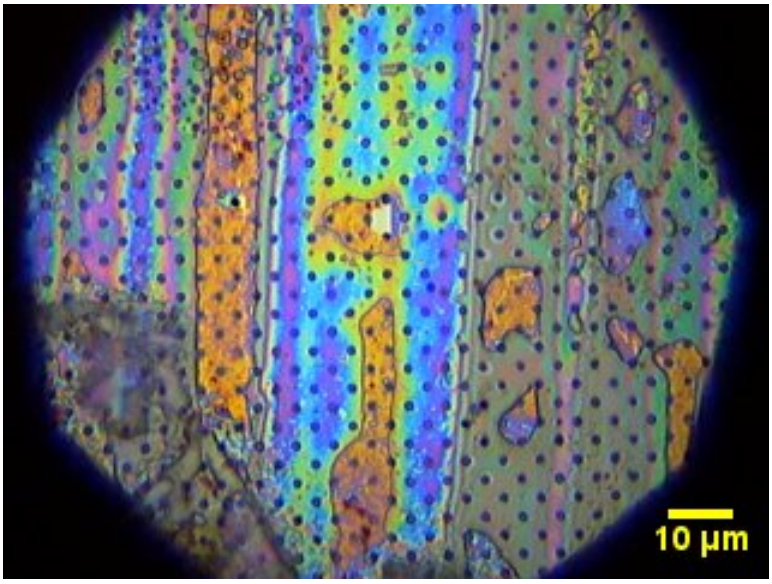

Figure 2.14: Result of a direct transfer of graphene. Graphene is present on the surface, but only in the blue coloured areas. The colouration indicates very thick membranes. This is not acceptable as the experiment requires a thin graphene membrane. This also indicates the presence of contaminants on the sample.

2.4 Results

The purpose of growing and transferring graphene was to have better access to new interesting samples for electron holography. Currently the samples are obtained from the Naval Research Lab in Washington, DC. The samples are grown and transferred by Jeremy Robinson at the Naval Research Labs in Washington, DC.

The system currently uses a partial pressure method to grow single layer graphene. The copper samples are characterized in Raman spectroscopy to identify whether the growths are successful. Once identified, the graphene is transferred to a gold-coated silicon nitride TEM grid using a standard technique (figure 2.13).

The wet transfer method appears to be the most reliable method. The method only recently became successful, mostly because sample handling techniques have been refined. The dry method, though still a potential candidate, has been far less succesful, with only trace amounts of graphene being present.

There are still remaining issues with the process of growth and transfer of graphene. The single crystal regions for the graphene growth method used in this study are known to be quite small. A different method, where the copper is folded over and crimped to create a copper enclosure. The carbon diffuses through the copper to grow on the inside of the enclosure. This method is known to produce higher quality graphene.[55] Currently, the method of partial pressures is used to grow the graphene. Soon the leak valves will be replaced with more robust flow controllers that will allow for finer tuning of the growth

process. As of yet no sample of grown and transferred graphene has been put in the system. The quality of the graphene in comparison to the NRL samples will have to be measured.

Further studies of transferred graphene on TEM grids are planned. The STM of freestanding graphene, which was difficult due to its thermally excited vibrational modes, has recently been shown.[50] Our instrument, designed to be able to obtain holographic and STM images, could provide images of freestanding graphene using both techniques. There are some potential experiments which use both PPM and HREELs to study the phonon excitation in suspended graphene. Methods to damp the vibrational modes at low temperatures is another potential avenue of study. The nature of graphene is a field of study that could yield many more discoveries.

Chapter 3

Point Projection Microscopy

To achieve high resolution in electron holography, the source must be highly coherent. The most coherent sources of electrons are fabricated on the atomic scale.[10] The tips require low pressures to produce stable beams.[56] An ultra high vacuum (UHV) chamber is used to achieve isolation from atmospheric pressure.

The UHV system, designed and built by Josh Mutus, houses a number of tools required for electron holography experiments. The system has three chambers: the loadlock, preparation and main. The loadlock chamber provides access from the outside world to the system. At ambient pressures, tips and samples will become covered in monolayers of contaminants. The preparation chamber serves as an area where dirty tips and samples can be modified without affecting the pressure in the main chamber. In the preparation chamber, tips can be both cleaned and etched in an isolated environment. The main chamber is where the holography experiments take place and has been specially designed to reduce the presence of stray magnetic fields, which could alter the electron beam. The UHV system has also been designed to damp vibrations.

A vibrating tip produces overlapping holograms: this washes out the high-order features. The UHV system has a number of levels of vibration damping. The floor which the system is built is isolated from the rest of the building and is also supported by layers of concrete. The system is supported by three STACIS active legs that are used to further damp vibrations within the range of 20-200Hz. Finally, the scanning head in the main chamber is hung from the top of the chamber using viton rubber cords, which have been shown to have favorable damping properties. A more in-depth description can be found in a previous dissertation.[11] In this chapter, the methods for preparing tips and performing electron holography experiments will be discussed.

3.1 Tip Preparation

The limiting factor in electron holography is the spatial coherence of the source. A source with a small radius of curvature provides a small virtual source size which is directly related to the resolution of the instrument. Cold-cathode emission tips, developed by Crewe, were

the first attempts at creating a source with a size on the order of tens of nanometers. These tips became the foundation for new techniques to push the limits of coherence. Fink showed that by using field ion microscopy (FIM), SATs could be built by depositing atoms on the apex of an electrochemically etched tip. The tips showed high brightness and were fully coherent. They were, however, limited to an opening angle of 3^o[8], which is insufficient for high resolution. Further research showed that the aspect ratio of the tip plays a key role in the opening angle in cold-cathode emission.

A new method to prepare SATs was introduced in 2006. This method uses a field-assisted etching process in FIM. The process of etching removes atoms from (instead of building on top) the tip. The process depends on the local field, which gives the user control over what region of the tip is being etched. By controlling the voltage, the user can thereby control the aspect ratio of the tip. [57, 58]

SATs made from polycrystalline tungsten(110) have shown high coherence angles, which are as large as 14°, leading to a resolution of 1.6 Å.[35] Single crystalline wire was suggested as a medium to further extend the coherence of the source. W(111) is easily etched by the field-assisted etching process, making SATs more reproducible than when using its polycrystalline counterpart. W(111) is a soft material which is easily damaged by handling, unlike W(110) which is mechanically robust. A combination of the two materials is used to obtain a workable source, which also has the desired etching properties. The two materials are spot-welded together such that a small amount of W(111) extends from the bulk of the combined tip.

The following process is used to create a hybrid tip: First, a 13.5 mm length of straightened W(110) wire with a 0.01" diameter is cut and 5 mm of W(111) 0.005" wire (figure **??**). The wires are cleaned by placing them in a small vial of IPA for 20 seconds. Once clean, the wires are removed and dried using Kimwipes. A copper block, which serves as the anode, has a number of grooves that allow the wires to remain fixed during the process (figure 3.1a). Scotch tape is placed on the block to ensure the that current from the cathode passes through the wires instead of directly from one terminal to the other. The thinner wire is placed on the block first to keep the wires aligned during spot-welding. To ensure no W(111) is wasted, the overlap between the two wires is kept to 1 mm. The Unitek welder is switched to the high setting and dialed to $4.8W \cdot s$, or 8%. To spot-weld, the cathode is placed on top of the W(110) and a small amount of pressure is applied. The cathode is a long cylinder of copper covered, by a rubber sleeve, which has a small bare section at the top (figure 3.1b). Once the wires are properly aligned, the power supply is activated using a foot pedal. The tip is spot-welded several times to ensure a successful bond. To check the strength of the bond, the 110 wire is held with a pair of tweezers while a second set of tweezers is used to apply force outward on the 111 wire. The result of a successful spot-welded tip is shown in figure 3.1c.

The tip for the field-assisted etching technique must be sharp enough to be imaged in

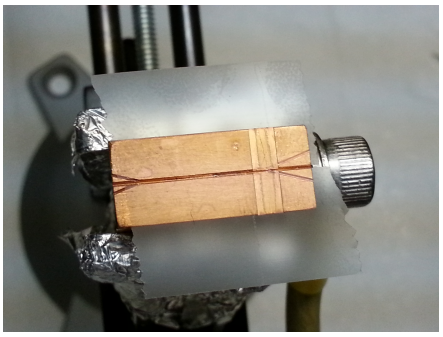

(a)

(b)

(c)

Figure 3.1: a) Copper anode used in spot-welding of hybrid tips. The Scotch tape is to ensure the current passes through the wires. The grooves in the electrode keep the wires steady during the process. b) Copper cathode used in spot-welding. The shaft of the copper is insulated with rubber to protect the user. c) is the result of a successful spot-weld.

FIM. To prepare a tip, it must be electrochemically etched in a $2M$ NaOH solution. In the electrochemical reaction, the tip serves as the anode and small metal filament is the cathode. The terminals are partially submerged in the solution and a voltage is applied across them (figure 3.2). The reaction occurs preferentially at the meniscus on the tip, which provides a cusp shape. The wire will eventually break near the interface and the lower part will drop off, leaving behind a tip with a 10 to 20 nm radius of curvature. The reaction is halted when the tip breaks at the meniscus. The tip breaking cause a significant change in the current. The circuit is designed to open when the change in current is large enough.

To prepare a tip for FIM that can be reproduced multiple times, the following procedure is used: To remove amorphous contaminants from the spot-welding process, the interface of the weld is submerged and etched for two seconds. The tip is then withdrawn from the solution until only 3 mm remain in the etchant. The electrochemical reaction is allowed to progress until it is automatically halted by the power supply, in about five minutes. Once the process is terminated, the tip is submerged in DI water to remove any residual NaOH. The tip is studied optically at 50x magnification to ensure that it is sharp. If the tip is deemed to be dull it is discarded, otherwise, the tip is ready to be loaded into the UHV system for further etching. Before etching, the tip is resistively heated to 700°C for 2

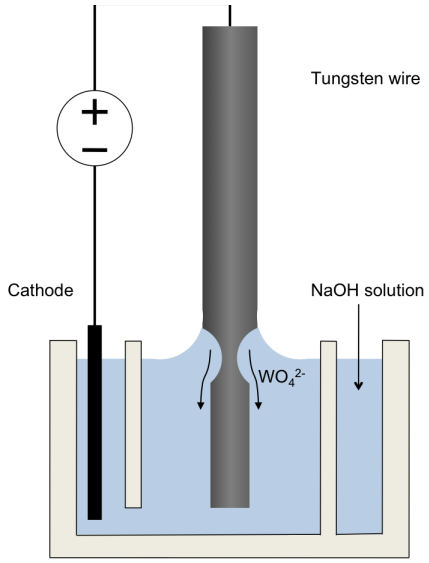

Figure 3.2: Schematic of the electrochemical etch process for W tips. The tip (anode) is submerged in solution and allowed to etch until the bottom drops off creating a tip with a radius of curvature of approximately 20 nm, which is insufficiently small for electron holography.

minutes to remove any lingering contaminants.

Once cleaned, the tip is placed in the FIM holder and brought close to a microchannel plate (MCP), which serves as a method for detecting ions. The MCP also amplifies the signal. The outgoing electrons are converted to photons using a phosphor plate. The photons are then captured by a camera mounted to the system. The camera mount was designed to be rigid such that the camera remains stationary with respect to the position of the MCP (figure 3.3). The mount also occludes ambient light, which is a source of noise.

The procedure for etching a SATs is as follows: To begin, the tip is brought within 1 cm of the MCP. The front of the MCP is then turned on and set to -1600V. The back of the MCP is set to ground. Finally, the phosphor plate is set to 2200V. To reduce the number of sources of ions, the ion gauge and ion pump are isolated from the MCP. The imaging gas, helium, is then leaked into the system at a partial pressure of $1 * 10^{-5}$ Torr. A relatively small positive bias – usually 1000 V – is placed on the tip. To avoid damaging the tip, the voltage is slowly increased until an image of the apex is visible. This usually occurs at around 10-15 kV, depending on the tip's curvature. The voltage is increased until the apex begins to field evaporate, a process which strips atoms from the apex due to the high field, in order to bring the tip to a common starting point for etching. Tips can be easily reproduced if they are brought to a common starting point of an atomically clean ordered FIM image.

Once the tip has been sufficiently evaporated, liquid nitrogen is flowed through the FIM holder to increase the stability of the atoms on the apex. To obtain a clear image of the tip, the voltage is decreased to 80% of the voltage required for evaporation. This is called

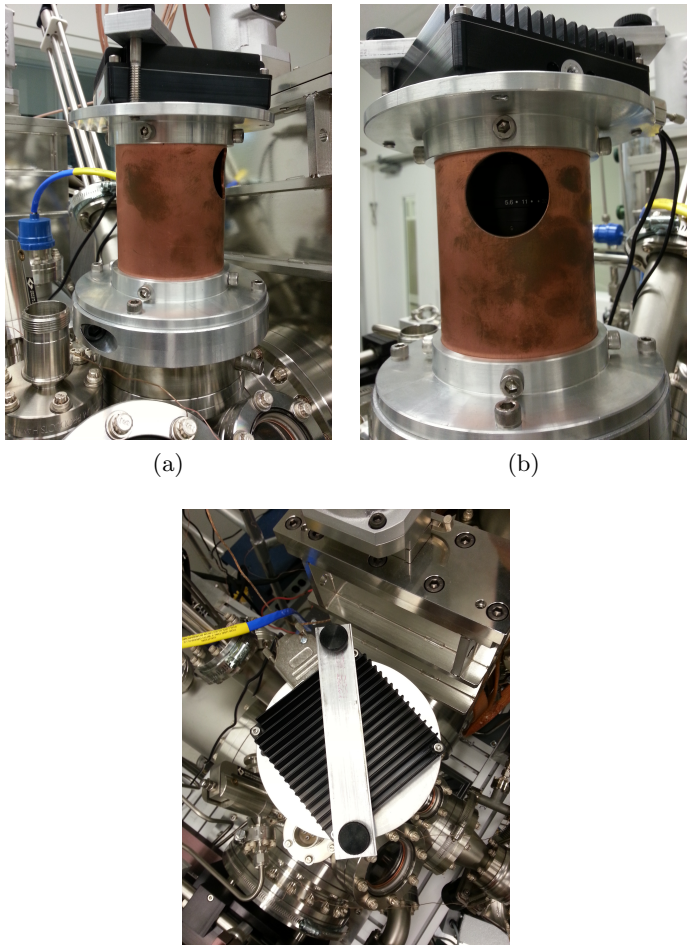

(a) (b)

(c)

Figure 3.3: Camera mount designed and built in conjunction with Mark Salomons at the University of Alberta. The purpose of the new mount is to reduce the amount of ambient light recorded by the camera. A port in b) is used to manipulate the settings of the lens. The camera is clamped to the mount such that the perspective of the images remains the same for any given experiment.

the imaging voltage. A background pressure of nitrogen is leaked into the system at a partial pressure of $2 * 10^{-6}$ Torr. A pre-etch is used to further clean the shank of the tip by decreasing the voltage at a rate of 1 V/s for 1000 seconds. Once the pre-etch has finished, the voltage is ramped back up to its original voltage at a rate of 10 V/s. The pre-etch is typically run twice to ensure that the shank is clean.

Once the pre-etch is complete, the tip is returned to imaging voltage and the etch can begin. The voltage is lowered at $1V/s$ until it reaches $5.5kV$ and only the apex can be seen. The nitrogen pressure is reduced to $5 * 10^{-7}$ Torr to slow down the etching of atoms. The voltage is dropped at the same rate in $100V$ increments to ensure that the end point is not overshot. Once the etching is complete, the nitrogen valve is closed and the voltage is then reduced to zero. The tip is allowed to reach ambient temperature over the course of an hour before loading into the main chamber. Figure 3.4 shows time sequence of an etching experiment.

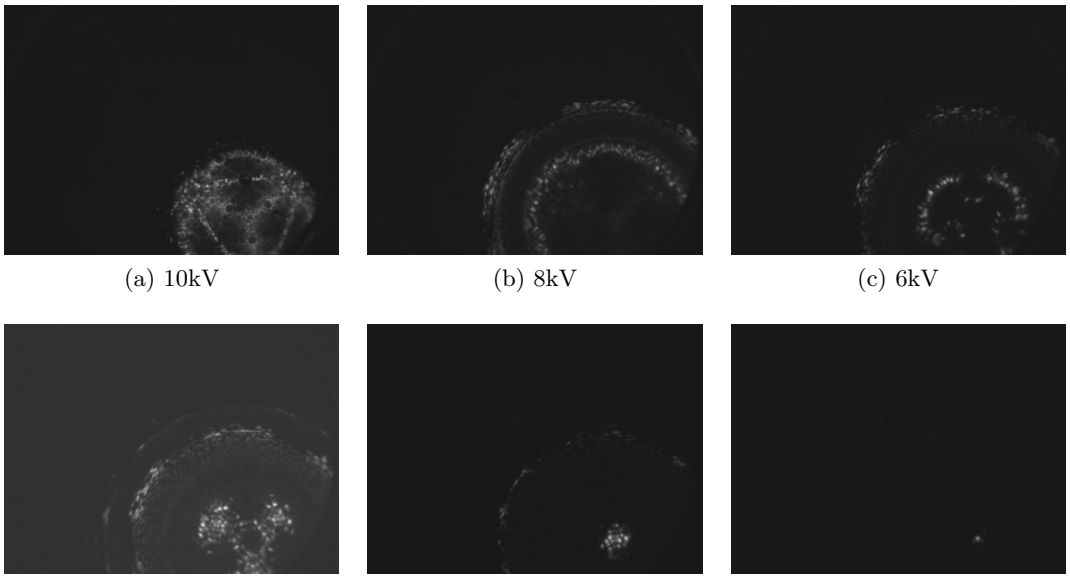

(a) 10kV (b) 8kV (c) 6kV

(d) 5.5kV (e) 5.2kV (f) 4.9kV

Figure 3.4: Image sequence of a W(111) tip etch in FIM.

3.2 PPM images

Accumulation of contaminants can cause the sample to become opaque when examining with a low energy beam.[23] Before the sample can be loaded into PPM, it is cleaned using resistive heating. The temperature of the sample is brought to 500^oC causing an increase in pressure due to evaporating contaminants. The temperature is held constant until the chamber recovers to base pressure.

Once a tip and sample have been prepared, they are ready to be loaded in the main chamber. A macro alignment of the tip and sample is used to ensure fast identification of

the grid in PPM. The MCP voltages are set to ground, 1600V and 3000V. With the tip fully retracted, the voltage is increased until the grid becomes visible, usually -500 V. The grid will appear as an array of circular bright spots amongst a noisy background (figure 3.5). To find an appropriate sample, the image is magnified by decreasing the tip-to-sample distance using the coarse movers until individual pores can be distinguished, $\approx$ 50 holes per image. When moving the tip, whether laterally or approaching, the voltage must be decreased to the point where the image on the MCP is barely distinguishable. This prevents drastic changes in tip current, which could have an adverse effect on its structure. Once the desired sample is found, the magnification is increased until the pore covers the entire detector. A more in-depth instruction for using the PPM can be found in a previous dissertation.

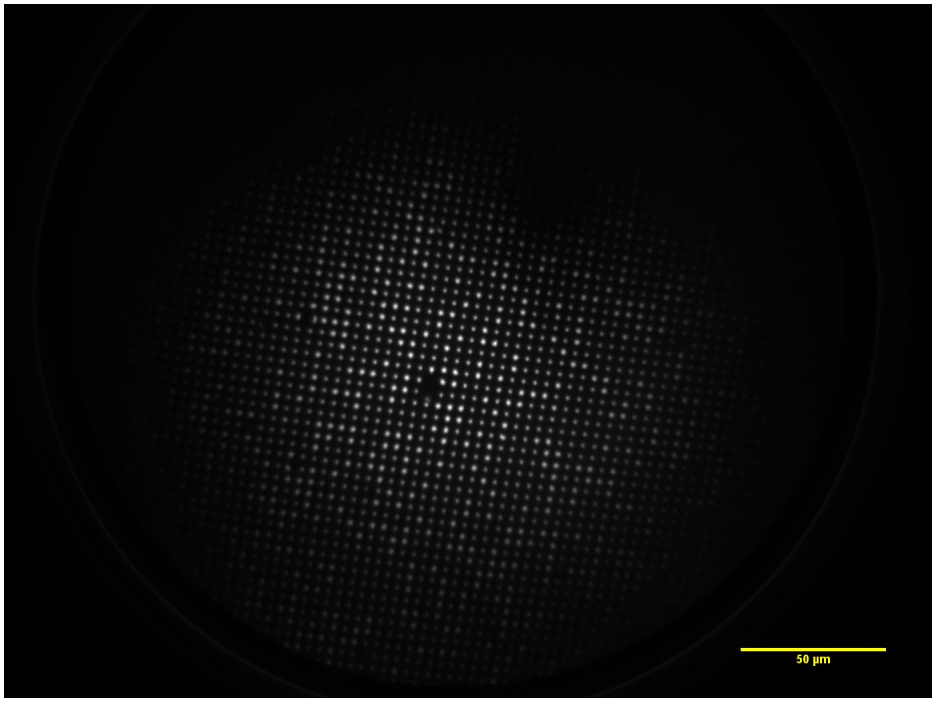

Figure 3.5: An example of how the grid appears on the detector fully zoomed out (D=70 mm) at -500 eV.

The pore provides a reference for calculating magnification by comparing the size of the detector, 27 mm in diameter, to the size of a pore, 2 μm in diameter. After measuring the total diameter of the MCP and pore in pixels, the magnification is calculated using:

$$M_{ref} = \frac{p_{pore}}{p_{MCP}} \frac{W_{MCP}}{W_{pore}} \tag{3.1}$$

where p is the number of pixels and W is the width in mm.

Calculating higher magnifications is achieved by measuring the change in size of a feature present in both the reference image and new image. The change in size of the feature provides a factor by which the magnification has increased. The equation for calculating the increased magnification is as follows:

$$M_{new} = M_{ref} * \frac{f_{new}}{f_{ref}} \tag{3.2}$$

where f_{new} is the feature size (in pixels) for the fully magnified image and f_{ref} is the feature size in the reference image. Figure 3.6 provides an example of the calculation of higher magnifications.

Figure 3.6 (a) is the reference image because the perimeter of the hole can be seen. The magnification in the reference image is $9.0{\cdot}10^3$ times. The feature in (a), measuring 133 pixels, is deliberately small in order to make it easier to measure large increases in magnification. In (b) the same feature is 215 pixels. Using equation 3.2, the new magnification is $1.5{\cdot}10^4$ times.

3.3 MCP Dark Spot

PPM images from the previous section all have a spot where the intensity drops to zero, despite being within the beam profile. The dark spot will remove information about the wavefront at that spatial location. The loss of information will be reflected in the reconstruction of the hologram. To obtain the best holograms possible, the process of forming the dark spot must be understood.

Dark spots can be caused by different mechanisms, such as a damaged MCP or an object between the tip and detecter which is occluding an area of the detector. When an MCP is damaged the area becomes unresponsive to incoming electrons and thus produces no outgoing photons. Damage to an MCP can be caused by mishandling the detector before mounting, or by improper cleaning techniques during successive use in UHV. A dark spot can also be caused by an object lying somewhere between the source and the detector. This creates a shadow on the MCP, resulting in a low number of counts. The dark spots produced by the previous mechanisms, however, cannot explain the one seen here.

Figure 3.7 shows a sequence of images in PPM displaying the dark spot in different positions. This rules out the possibility of a damaged MCP, as the dark spot would remain stationary on the detector. For an object to occlude the beam, it would have to be located either on the sample substrate or the MCP. If the object were on the SiN substrate, the spot would become magnified as the tip approaches during a typical PPM experiment, which is not seen. A dark spot caused by an object on the MCP is also not a reasonable explanation, since the spot would remain stationary. To explain the presence of the dark spot, it is necessary to understand the technical information about an MCP.

The MCP is an array of parallel cells (arranged in a honeycomb pattern), which are comprised of two angled channels at 8° with respect to the normal, that form a chevron (figure 3.8). An electron is detected when it interacts with the side of a channel, which results in the production of secondary electrons. The voltage between each stage of the MCP provides a cascading amplification of the signal. If an electron were to pass through

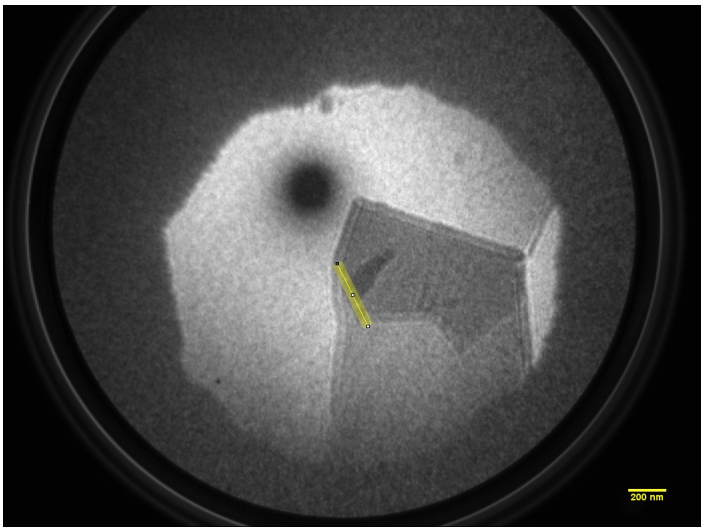

(a)

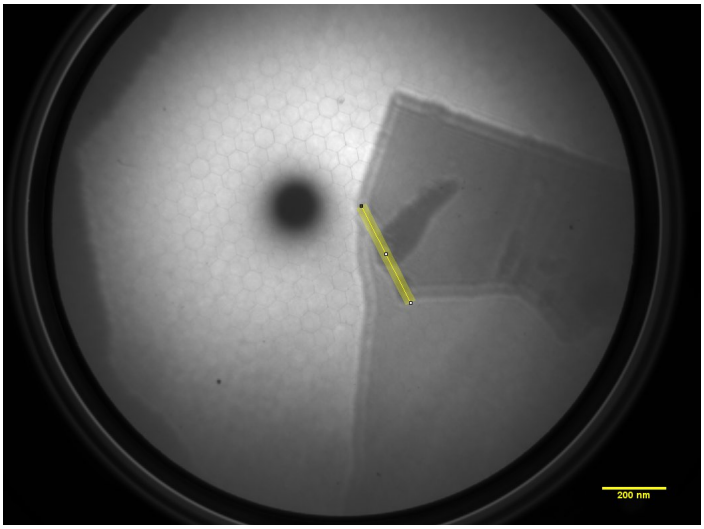

(b)

Figure 3.6: To calculate the magnification when a grid pore is no longer visible, a feature in a reference image (a) is compared to the same feature in a subsequent image at higher magnification. The ratio of the number of pixels gives the factor by which magnification increases.

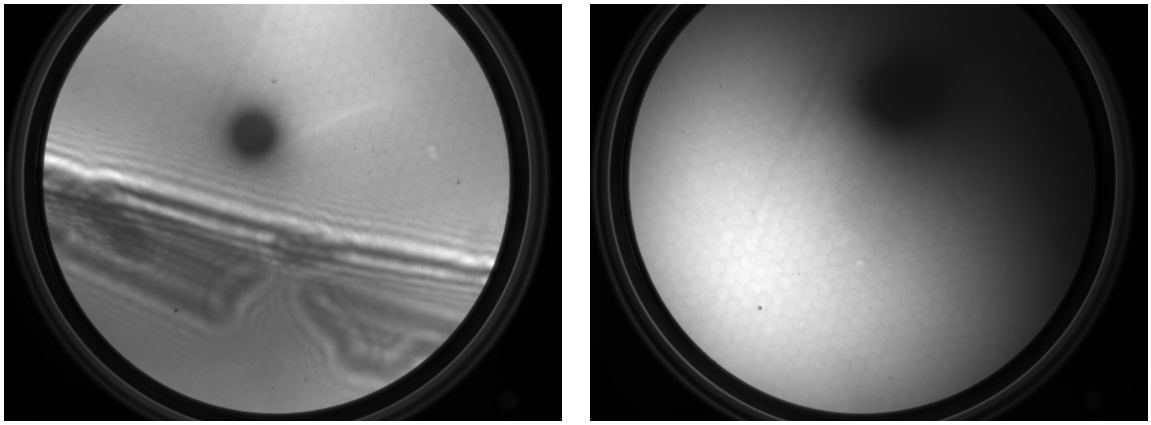

(a) (b)

Figure 3.7: MCP in PPM experiment. The position of the dark spot changes position depending on the set up of the system. This means that the dark spot cannot be a dead spot on the detector.

the first channel undetected, the amplification would be much smaller than that affecting the surrounding interactions. In order for electrons to pass through the first channel undetected, the angle of the electron with respect to the axis would have to be the same as the angle of the channel. If the opening angle of the source is greater than the angle of the channels, there must be an electron path such that this process occurs. In order to study this effect, a simple geometrical measurement is made.

If the dark spot is created by this effect, the radial distance of the spot should change with the distance of source and detector. The relationship between the source-to-detector distance and position of the dark spot is described by:

$$\tan\theta = \frac{x}{D}, \tag{3.3}$$

where x is the radial distance of the dark spot, D is the source-to-detector distance and θ is the angle of the electron with respect to the axis. As D is decreased, x must also decrease by the same factor (figure 3.9). This measurement can be reproduced in the microscope by changing the tip-to-detector distance in the chamber. To isolate the measurement of the distance x, the experiment is conducted with a constant tip-to-sample distance, beam energy and position of the beam. To align the beam in subsequent images, a reference marker on the capture software is aligned with a feature on the sample.

The center of the beam profile must be known in order to measure the radial distance of the dark spot. This is achieved by drawing a circle around the beam spot using a three-point technique. The three points, which are placed in regions of equal intensity, are connected to create an arc which can be used to draw a circle. The three points are selected where the beam drops to zero, allowing for consistency between measurements for multiple images. An example of the output from a three-point circular measurement is shown in figure 3.10.

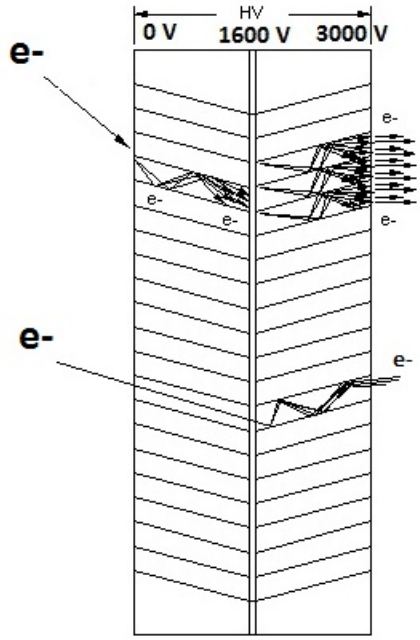

Figure 3.8: Simplified schematic of a MCP. The channels used for amplification of the signal are parallel across the detector. The signal is amplified when an electron strikes the wall of the channel to create secondary electrons. Electrons meeting the MCP at the sample angle as an individual channel will result in a much lower amplification, leading to a dark spot.

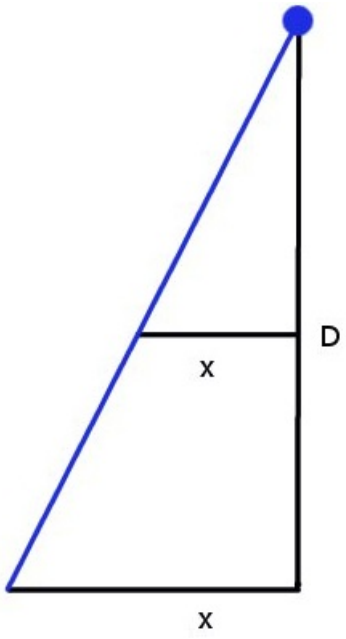

Figure 3.9: A schematic showing the affect of D on the position of the dark spot, x. The smaller D is, the smaller x must be. By varying D and measuring x, the angle of the channels can be calculated and compared to factory specifications.

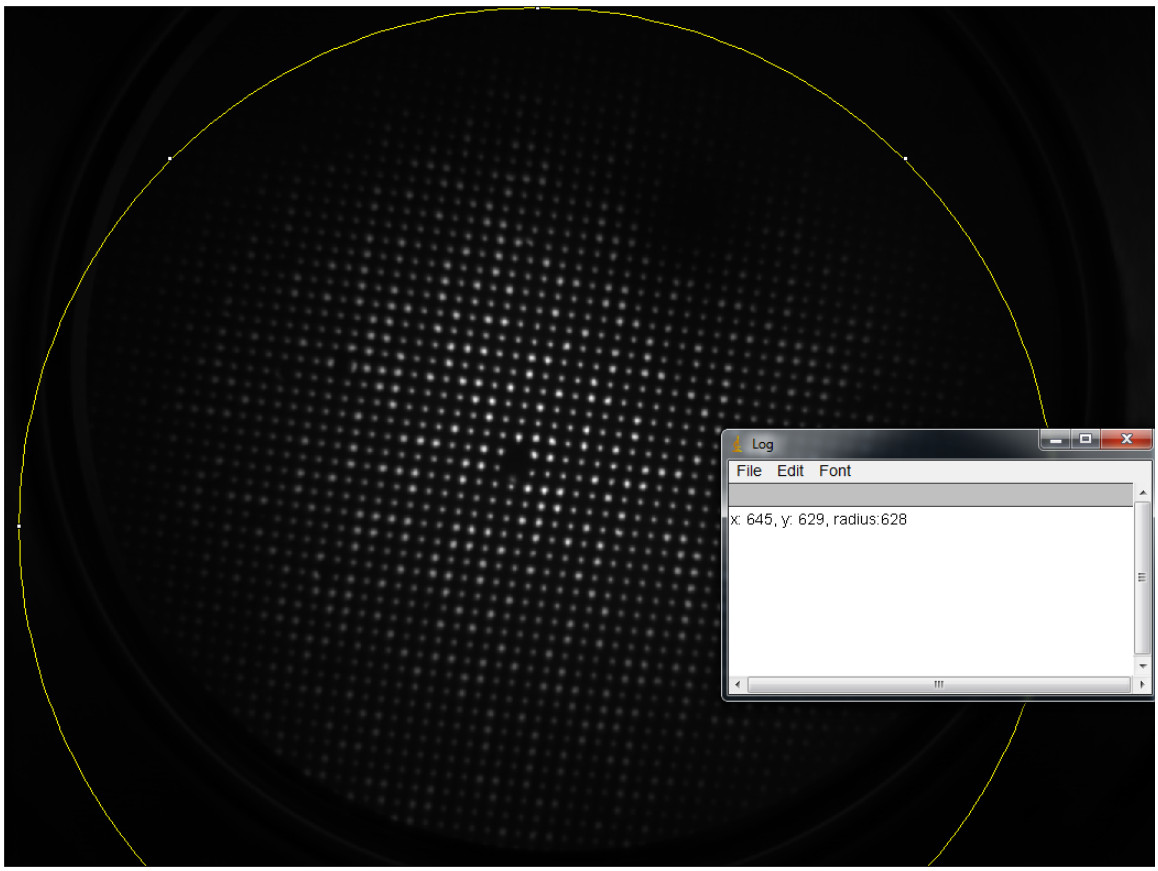

Figure 3.10: Example of the three-point method used to find the center of the beam and dark spot. Three points on the edge of the beam profile are chosen. An algorithm uses the three points to create a circle and find the center of the beam. The distance between the center of the dark spot and the beam is the value of x from figure 3.9.

Another circle is drawn around the dark spot to find its center. The distance between the centers is calculated. The resulting measurements are summarized in figure 3.11.

This shows that it is possible that the mechanism creates the dark spot. The measured angle from the specifications of the device is 8^o, while the measured angle of the channels is 6 ± 6^o which agrees within uncertainty.

Electron holography experiments require large opening angles to obtain high resolution images. Typical MCPs have channel angles at 8^o, and 12^o which are both smaller than the opening angle of the source used in the microscope. To avoid this issue, a special MCP with higher angles would have to be employed. This would require an increase in the size of the bezel due to the projection of the channel on the length of the MCP. Another possible solution is to angle the detector such that the angle of the channels is artificially increased. This would make reconstruction more difficult. Another possible solution is to create a radially symmetric MCP. Other solutions, such as direct electron measurement systems, are the subject of future work.

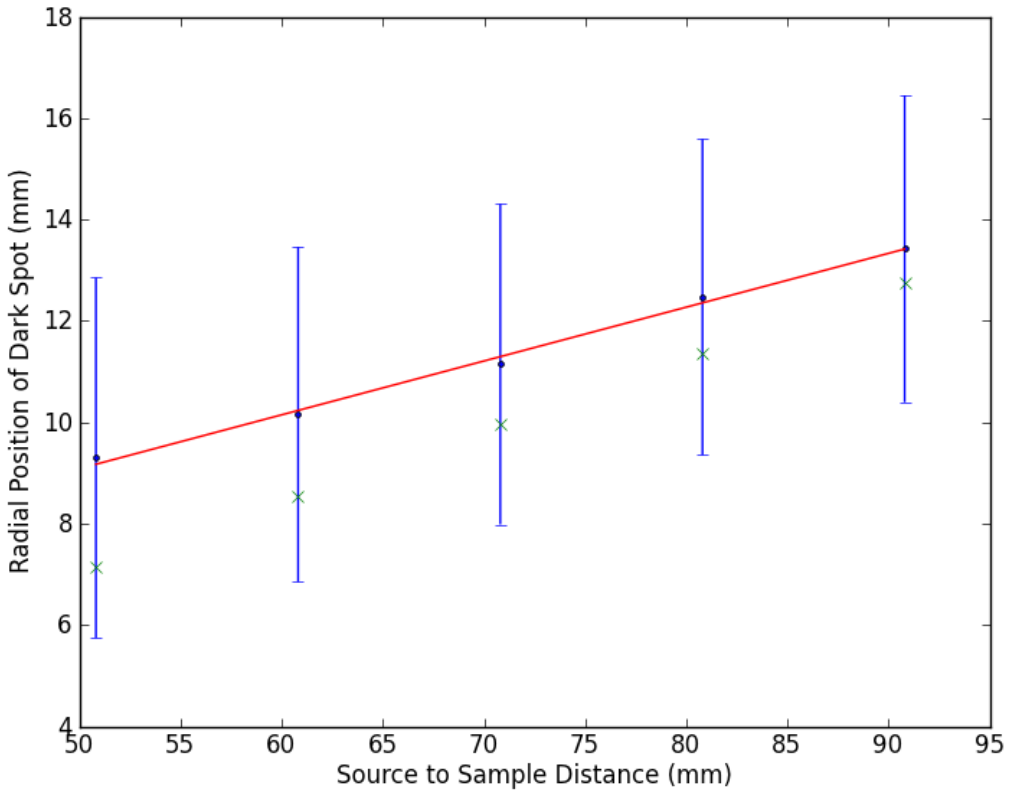

Figure 3.11: The resulting measurements of x (y-axis) for varying D (x-axis). The (blue) dots are the experimental data and the (green) "x" are the theoretical results for a channel angle of 8°. The experimental data leads to the result of 6 ± 6° which agrees within uncertainties.

Chapter 4

Image Capture and Processing

In the past, photo emulsions were used as a method for capturing images from an electron microscope. Depending on the application, it was found that varying the thickness of the emulsions and using different chemical treatments allowed for better contrast, which resulted in higher resolution images. However, photo emulsions could only be exposed once. Today, emulsions are rarely used. Digital technologies dominate for TEM, scanning electron microscopes (SEM) and electron holography.

For electron holography, the mode for capturing images is a charge-coupled device (CCD) camera. A CCD converts photons, which are emitted from the phosphorescent plate at the back of the MCP, into an electrical signal. A CCD camera makes it possible to capture many exposures using the same detector. The images are saved to a computer, which allows for easy manipulation and processing. This also allows for different processing methods to be used and compared.

The camera used in this study for imaging the phosphor screen, for both PPM and FIM, is a PCO 1400. The 1400 provides 14 bit image upconverted capture, 14 to 16-bit, 1392 x 1040 pixel resolution and a 65% quantum efficiency. The camera also provides a variable exposure time from 1 μs to 60 s and 7 frames per second capture speed.

4.0.1 Software

The holographic microscope is composed of a number of separate tools which require their own methods of control. A program was written such that all of the necessary tools for PPM and FIM could be monitored and, if possible, controlled. The program (Control) was written in LabView (LV) in conjuction with Radovan Urban of the Professor Wolkow's group at the University of Alberta in Edmonton. Figure 4.1 is the front panel of the Control program.

The majority of the front panel displays an image of the data being collected by the MCP. The front panel receives the images from a front-end open-source LV program provided by PCO. As the images are read they are upscaled from 14 to 16 bit to give the grey value a larger range. Though this does not create any more information than what is in the 12 bit

images, it does provide a larger range for analysing images while avoiding saturation. The program can edit all of the camera settings: exposure time, binning and imaging frequency. Exposure time allows the camera to average over a longer period of time if the photon count is low. Binning is used to reduce the file size of the image. In 1x1 binning, each pixel value is stored in the image, while in 4x4 binning, each point is an average of 16 pixels, reducing the resolution.

The control program was designed such that the images could first be visualized and then stored. The slider at the top of the control program allows the user to choose the maximum gray value. Any value above this maximum will appear white in the image. The full dynamic range is recorded. Control allows the user to adjust the contrast of the image being displayed. This is a useful aid used for visualization of data during an experiment. Images can be stored at a nominal 7 fps, though slower capture rates can be set as well, with varying number of averaged images.

There are two methods of averaging that can be used to increase the signal-to-noise ratio. Both approaches are based on a first-in first-out approach where images are added to an array until it is full. Once the array is full, the first image that was added is removed and a new image is placed in the array. The first method of averaging adds all of the images into the array together and then divides the pixel values by the number of images. The drawback to this method is that an individual pixel cannot exceed the maximum gray value allowed by a 16-bit image. If a pixel value exceeds the maximum, it is said to be saturated. Adding a large number of images together can cause regions to saturate, which would wash out features. The second method of averaging begins by dividing each image by the number of images within the array and then adding them together. This corrects for saturation but introduces the opposite effect. If the value of any given pixel is smaller than the number of images in the array, data will be lost. The first averaging method is typically used since a 16-bit image has a maximum value of 65536, which is much larger than the value due to an invidual exposure.

An image is saved by recording a "video" in the control program. First, the capture interval of the video is set at a value larger than or equal to 0.142 s, or 7 fps. The video begins to record when the "record" button is pressed. The process creates a new folder, labelled with a three-digit zero-padded number in sequential order, followed by a "File prefix" specified by the user. For example, with a file prefix "PPM", the first folder would be named "001 PPM". The capturing process also creates a log file both in the root directory, specified in the "Files" tab, that records all of the information monitored by the control program. The control program also monitors the source's voltage, current from the source, (xyz) position based on an arbitrary set point, images from the camera, frames per second, number of averages per image, averaging mode, voltage on the MCP and the given name of the source in use. The control program also provides a means of manipulating the system's power supplies.

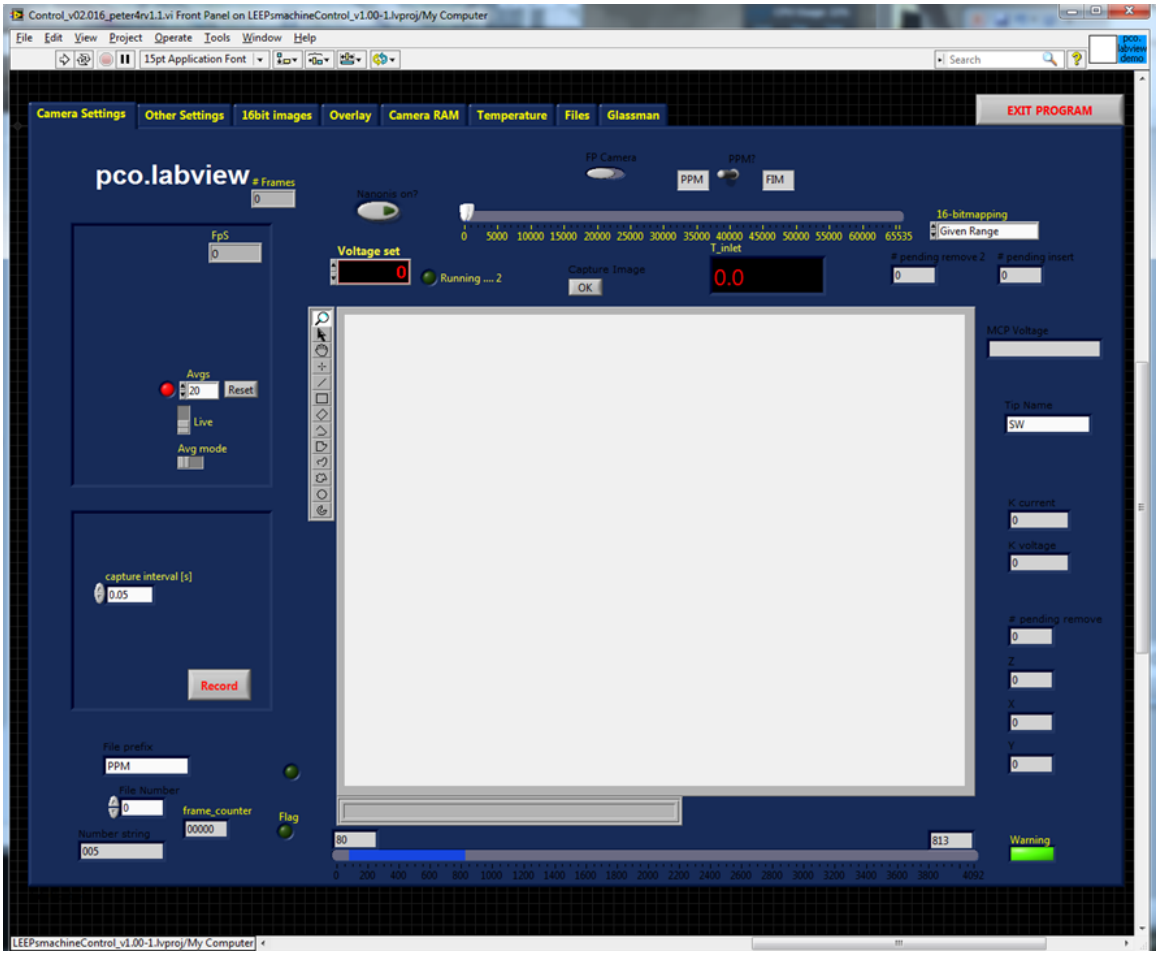

Figure 4.1: Control program written in conjunction with Radovan Urban at the University of Alberta. The program is able to monitor and control many parameters of the microscope such that they can be accurately recorded.

Depending on the current application, FIM or PPM, two different virtual instruments (VIs) – programs designed to interface with tools in the lab – are used. For tip etching, FIM, the Glassman tab in the Control is used. This tab allows the user to set ramp rates for etching, voltage pulse duration and size. Ramp profiles can be set by both the final voltage and time method or by setting a final voltage and a ramp rate in V/s. The voltage can also be manually manipulated from the front tab in Control under "Voltage set".

When control is in the PPM mode, a separate high voltage power supply is used (Keithley). In order to interface with this device, a separate program was written which sends information to Control using queues. Figure 4.2 shows an image of the Keithley power supply control program. The button on the lower left enables and disables the instrument's voltage. The dial is used to manipulate the value of the potential. The values of the minimum and maximum are changeable, even while the program is running, which gives the user complete control over the sensitivity of the instrument. The program can be further

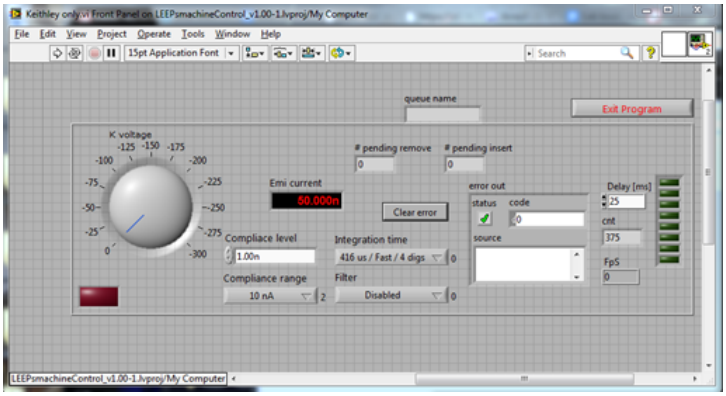

Figure 4.2: Keithley program which allows for the control and monitoring of voltages in PPM. The program also interfaces with the control program using queues.

tuned by setting the compliance level, compliance range, integration time and the filter. The compliance level is used to set a maximum current to protect the tip from currents that may alter the shape. The compliance range sets the sensitivity of the instrument for current monitoring. Integration time, like exposure time, specifies a time over which a value is measured, while the filter specifies the number of measurements made to average the final reading.

4.1 Image Processing

Digital capture is more powerful than its analogue counterpart due to the tools that are available for post processing. An image saved on a computer can undergo a number of different processing methods while retaining the original image. These processing methods include fourier transforms (needed for reconstruction) bandpass filtering (to reduce noise in an image), and resolution measurements. Digital capture also allows for many images to be saved in sequence which can be summed for increased signal-to-noise ratio.

4.1.1 Alignment

A single image has noise which is amplified by the two stages of the MCP. Direct summation of images is usually not possible due to the drift in the system. Image alignment is required such that features will not be washed out during summation. There are many programs available to align images based on feature recognition.

A program written by Mutus uses proprietary LabView (LV) functions to align images. First selects an area of interest and then it matches subsequent images by searching for the same area. This alignment process uses a translational alignment and outputs an x and y shift for each image. While this method can be effective, it is not overly reliable. Alignment tends to create sporadic shifts, because a hologram has a number of similar looking features: the fringes. By plotting the shift data, the drift in the sample can be seen in both the x

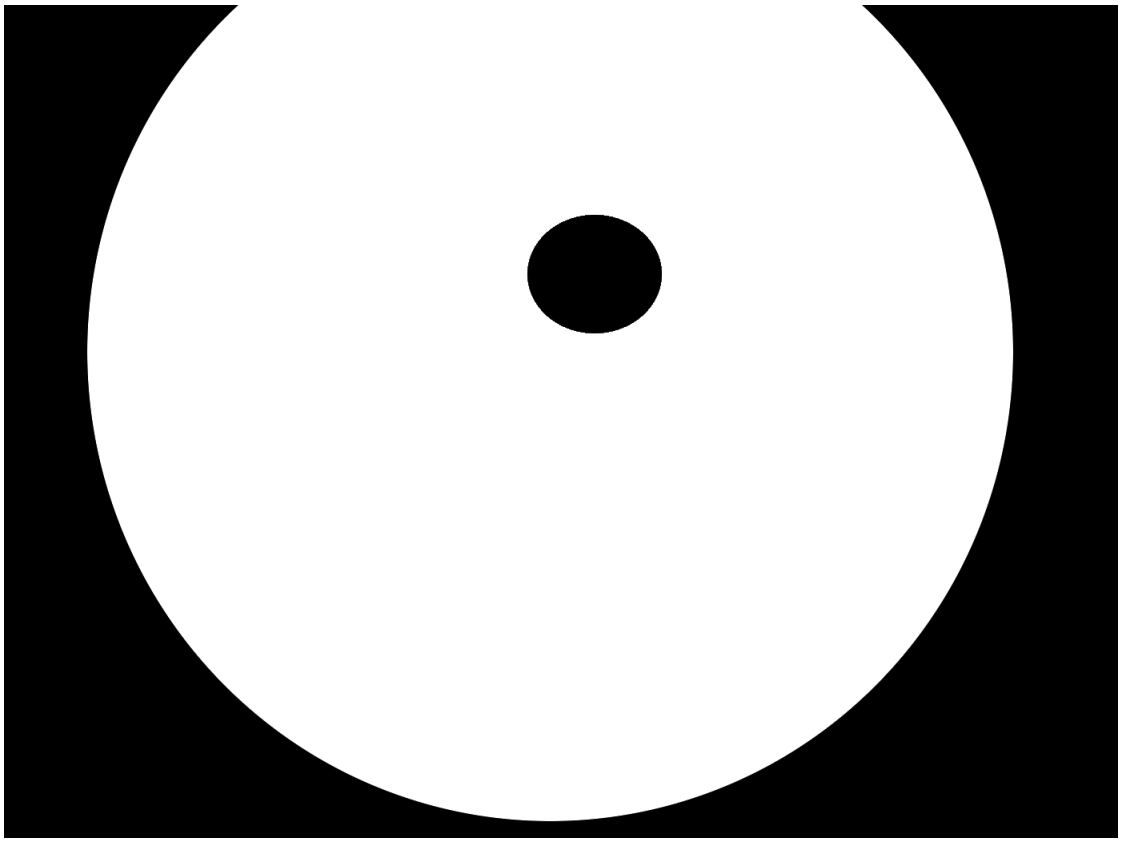

Figure 4.3: Example of a mask used in the i2k Align program. The mask is used to tell the program which areas to use during alignment. The black regions denote areas to be omitted during alignment. This allows the program to ignore features such as the dark spot or the edge of the MCP.

and y directions. To make the alignment more effective, the plots were fit using a second order polynomial. The shift values were calculated using the fit, and reapplied to the images during averaging. Unfortunately, this process worked for only a few samples, and the quality of the images increased very little.

More recent endeavors to increase the reliability of the alignment in captured images has turned the focus to proprietary software packages. There are many biology and astrophysics software packages. After sampling a number of programs, the one that stood out was i2k Align by DualAlign. The program is able to align holographic image features better than the other sampled programs. By using proprietary methods, i2k Align is able to align images using a translational transformation. One of the main features that i2k Align provides that helps with proper alignment is the use of masks, which allows the user to ignore particular features. For example, using a mask makes it possible to ignore the dark spot on the MCP in the alignment process (figure 4.3). Masks are binary images consisting of white regions (to be used in the alignment) and black regions (not to be used in alignment).

4.1.2 Analysis

Once the image set has been aligned, it is ready for analysis. The images are summed up to accentuate the features of the hologram, increasing the signal-to-noise ratio. With the use of an open-source program, ImageJ, it is possible to measure a hologram's lateral extent and the resolution of the reconstruction.

The resolution of a hologram can be defined in multiple ways. As stated earlier we can view a hologram as a lens used for reconstruction. The resolution of a microscope is most often characterized by the numerical aperture (NA) of the lens system in use:

$$R = \frac{\lambda}{2(NA)},$$

The equation above, taken from chapter 1, can be applied to a hologram. The NA can be described as half the opening angle of the lens, seen in figure 1.1. The analogous measurement for holography is half the total width of the fringe pattern. For a particular hologram, with a tip to detector distance L and a tip to sample distance d, this equation can be reduced further to known quantities of the system.

$$\begin{aligned} R &> \frac{\lambda}{2\sin\theta} \\ &> \frac{\lambda}{2\sin\tan\left(x/L\right)^{-1}}, \end{aligned}$$

where x is the width of half the fringe pattern and L is the tip-to-detector distance. The equation can be further manipulated to incorporate the deBroglie wavelength.

$$R > \frac{h}{2\sin\gamma\sqrt{2m_e eV}}, \tag{4.1}$$

where γ is half of the opening angle of the beam. Equation 4.1 describes a system limited solely by diffraction. Another widely accepted measurement of resolution is the virtual source size[10]:

$$R = \frac{\lambda}{\pi\gamma}, \tag{4.2}$$

where

$$\gamma = 2tan^{-1}(\frac{w}{2L}), \tag{4.3}$$

which describes the area of the source which is emitting electrons.

The issue with these measurements is that though they seem robust, there are no standard requirements for fringes. Take figure 4.4 for instance. The first fringes are easily visible; however, the higher order fringes quickly become lost to the noise of the detector. This lack of a standard could cause the resolution of the microscope to be either under- or over-estimated. The best method for obtaining resolution is to measure the reconstruction.

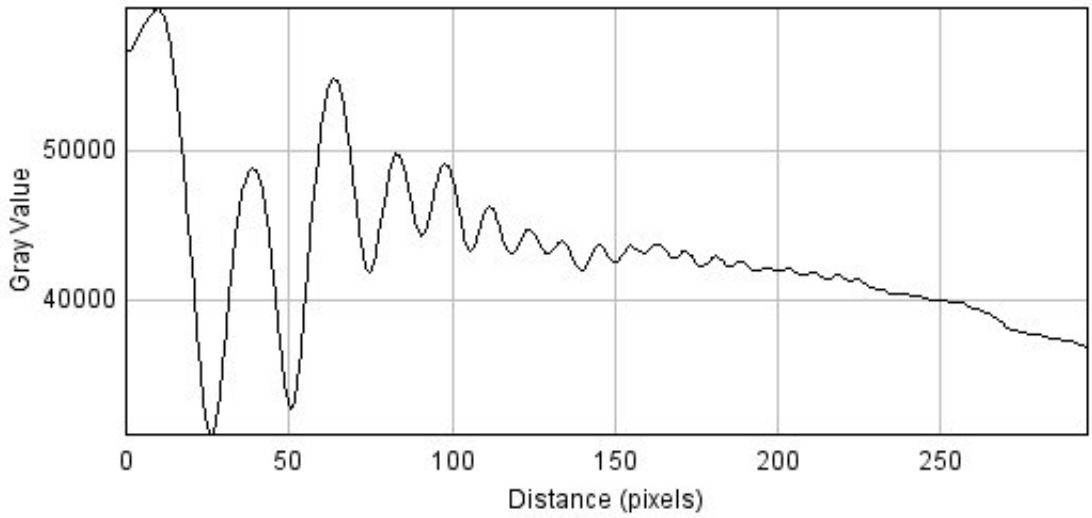

Figure 4.4: A typical line profile of a hologram. Initial fringes have a much higher visibility than the higher order fringes. It is hard to discern where the pattern ends, hence the under or overestimation of the NA of the system.

Originally, holograms were reconstructed using optical means. Today, reconstruction is achieved by solving the Kirchoff-Helmholtz equation, which is shown in Chapter 1.

$$\psi(\mathbf{r}) = \int_{Screen} ds_x ds_y I_{holo}(\mathbf{s}) \frac{\exp(iks)}{s} \frac{\exp(-ik|\mathbf{r}-\mathbf{s}|)}{|\mathbf{r}-\mathbf{s}|},$$

In order to reconstruct a hologram, all the system's paramters – tip-to-sample distance, sample to detector distance, wavelength, and the relative position of the sample with respect to the optical axis – must be well defined. The parameters enable a program, written by Lucian Livadaru of Professor Wolkow's group at the University of Alberta in Edmonton, to back-propagate from the hologram and obtain amplitude or phase reconstruction for a plane perpendicular to the optical axis. Figures 4.5 and 4.6 show the windows used in reconstruction.

The program's output is two jpegs, which are the amplitude and phase reconstruction of the object. In most cases, the object is considered to be an amplitude object (an opaque object with a large scattering cross section), and the appropriate reconstruction is chosen for further measurements. Figure 4.8 shows an example of a hologram and an amplitude reconstruction. Despite the program's robustness, many issues still need to be addressed.

The simplest method of measuring the resolution of a reconstruction is a sharpness measurement. The resolution is obtained by measuring the distance that it takes the contrast to go from 90% to 10% of the maximum contrast value.[59] This is limited by the minimum value of contrast for distinguishable particles given by the Rayleigh criterion of coherent light, 36%.

The process for calculating resolution is as follows: To begin, figure 4.7 shows a 1D cross

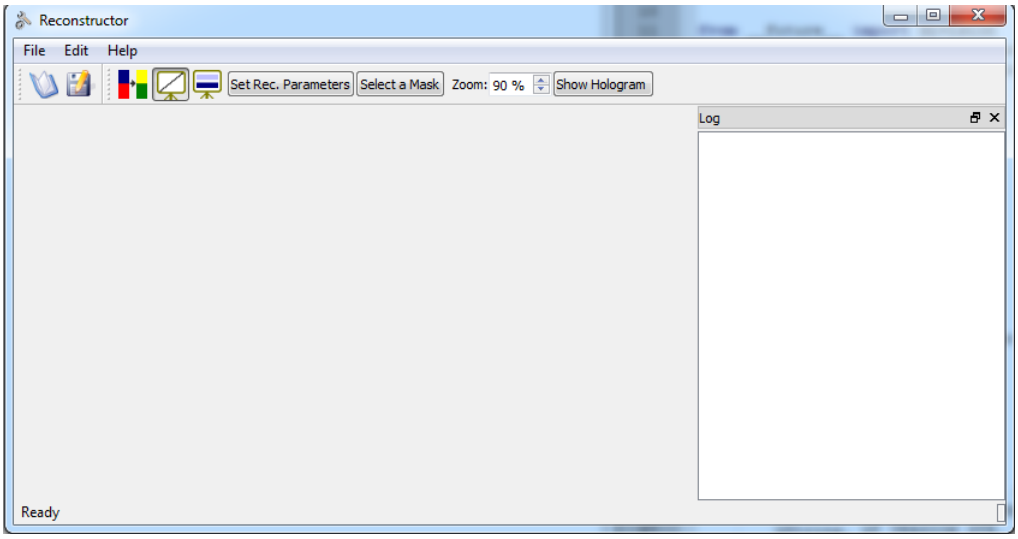

Figure 4.5: Reconstruction program graphical user interface. Written by Lucian Livadaru at the University of Alberta.

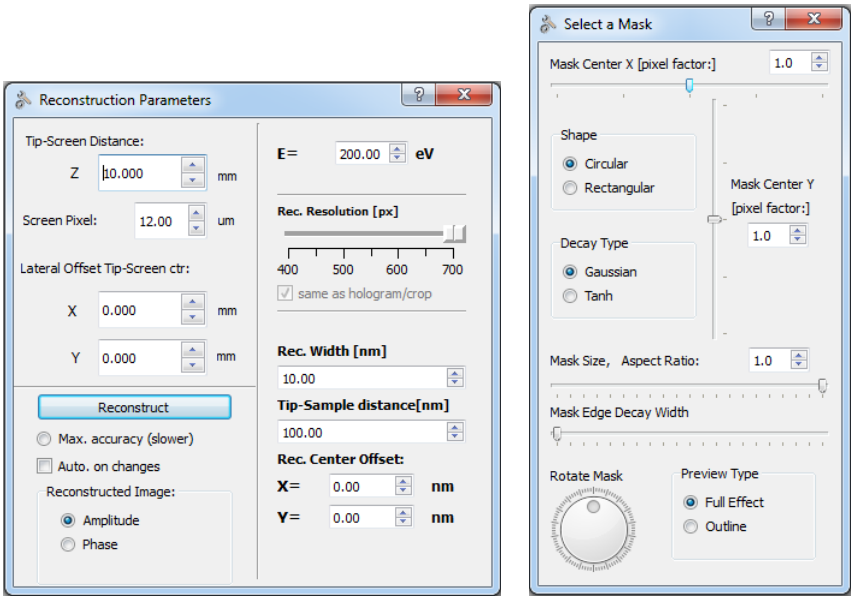

(a) (b)

Figure 4.6: a) Reconstruction parameter window. b) Mask window, used to apply a mask to the image to suppress fourier ringing.

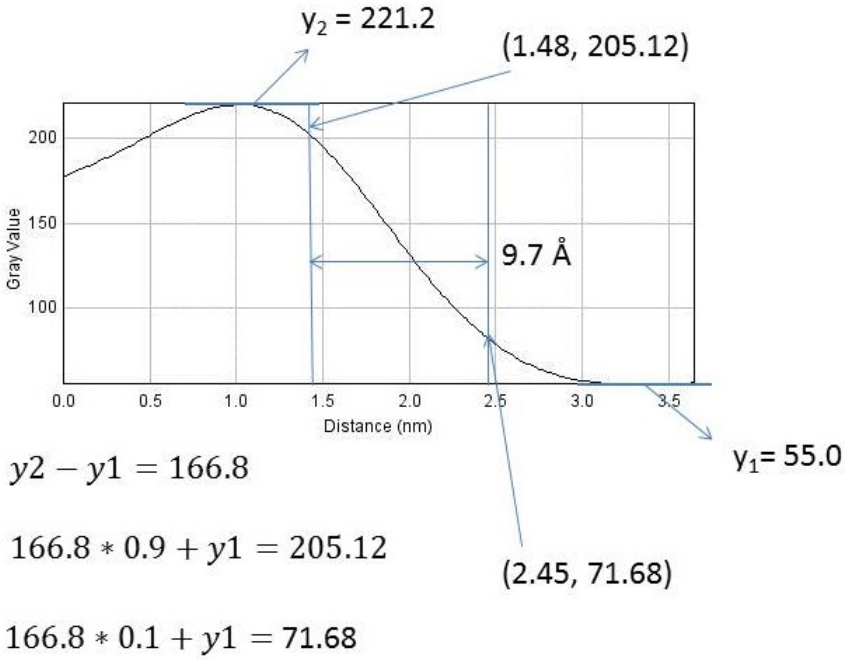

Figure 4.7: An example of how a sharpness measurement is carried out. The resolution is the distance between the 90% and 10% of max values of contrast.

section of a hologram along the sample's edge. The maximum value of contrast is 221.2 and the minimum is 55.0. To normalize, the difference between the values is calulated, 166.8. The 90 and 10% values are found and by measuring the change in x axis, a resolution can be found. For this measurement, the resolution is 8.2 Å. This method assumes a knife edge sample and underestimates the resolution, because electrons will eventually pass through the sample without interacting. Though this method is rough compared to the previous method, it provides a standardized upper limit to the resolution of the image.

The most noticeable issue is the twin image problem. Due to system's geometry, when an object is reconstructed at a distance d from the tip, there is also a conjugate image at $-d$ of the same object.[60] In many cases, this is not an issue, since d is large enough that the twin image is very out of focus. However, since d is small for the purpose of obtaining high magnification, the effect of the twin image is not negligible. Figure 4.8 shows an example of this. The bulk ringing which emanates from the object is the effect of the twin image being close to the object. There are many different proposed algorithms to alleviate this effect through an iterative process.[60, 61] Adding twin image correction to the program is the subject of further study.

Another major issue for the system is background removal. The background, or reference beam, needs to be removed from the image to fully isolate the cross term in equation 1.5 from Chapter 1. Initially, when studies were conducted without graphene, the pores played a larger role in extracting the electrons. Any irregularities in the pore with respect to another

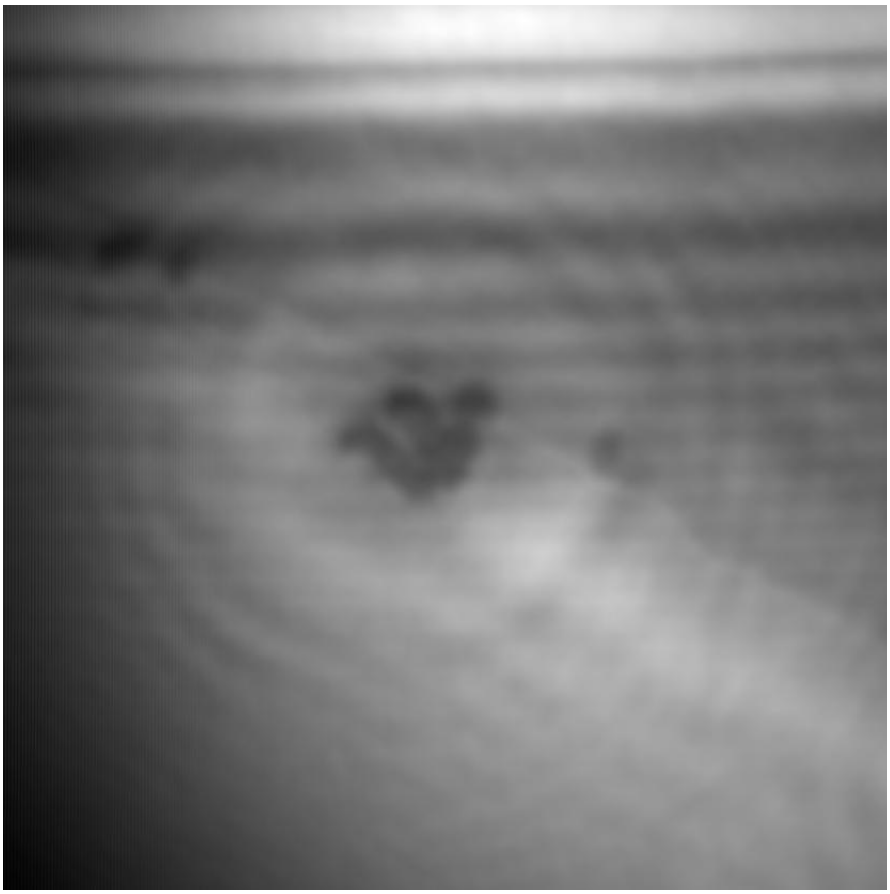

Figure 4.8: The twin image problem in a reconstruction of a defect on graphene. The bright rings around an object is the out of focus secondary image which is 180° out of phase. Due to the small length scales, its contribution to the reconstruction is not negligible. The object was reconstructed at d=1.8 μm, D=70 mm and λ=1.1 Å.

pore altered the beam led to discrepancies in the background. Attempts to simulate the background using Gaussian distributions have been explored, though with limited success. To obtain a background image, a blank (fully covered in graphene) pore is located. The tip is brought close to the surface and the voltage is increased to the imaging voltage (80-200 V). A number of backgrounds, for varying voltages, is taken in order for the field to be as similar as possible to the hologram. This use of graphene should alleviate the issue and is the subject of further study.

Obtaining the background of the image will also facilitate the calculation of the point spread function (PSF). The PSF describes how the system elongates a point object in both the transverse plane and longitudinal direction. The elongation is inherent in the microscope. Using a deconvolution process, the image can be corrected for the PSF, allowing the object to be more accurately reconstructed. The PSF also makes it possible to calculate the contrast transfer function (CTF). The CTF is a well-accepted method of calculating the resolution of a TEM microscope, a technique that would help further the standardization of measurements in point projection electron holography.

4.2 Case Study: Graphene

Graphene is placed on a TEM grid to provide a transparent support for samples and an equipotential plane for field lines. Graphene is an ideal substrate for the initial characterization of the W(111) tips. Previous work done by Mutus[11] provides a means of comparing W(110) to W(111) tips. Holography also provides a method to further study graphene. To prepare for imaging, the sample is heated to 500°C for one hour or until the chamber reaches base pressure to remove physisorbed species. Though the coverage percentage is high, there are regions where there is no graphene. A small fraction of pores are partially covered, leaving a vacuum graphene interface to be studied: a knife edge. The knife edge is a commonly used as a holography example in optics textbooks. However, the graphene is not opaque causing some deviation from the model of a opaque knife edge. The low electron attenuation of the graphene allows the reference beam to pass through the graphene, creating wide fringe patterns with lower contrast.

Though most pores are completely covered in graphene, it is not difficult to find a knife edge. An edge is found when the amount of signal within a pore has two distinct values (figure 4.9). Once found, the tip is brought closer to the sample to increase the magnification until the image of a single pore covers the entire detector.

To compare W(110) and W(111) tips, a previously collected hologram from [11] and a hologram with similar parameters are summarized in table 4.1. The resolutions, calculated using the diffraction limit (equation 1.1), are very similar. The difference in resolution could be due to a number of factors. This is an example of a tip which terminated in three atoms. A single atom tip would be expected to show an increase in the lateral extent of the hologram. Improved skill in tip preparation will allow for preparation of sharper SATs. The

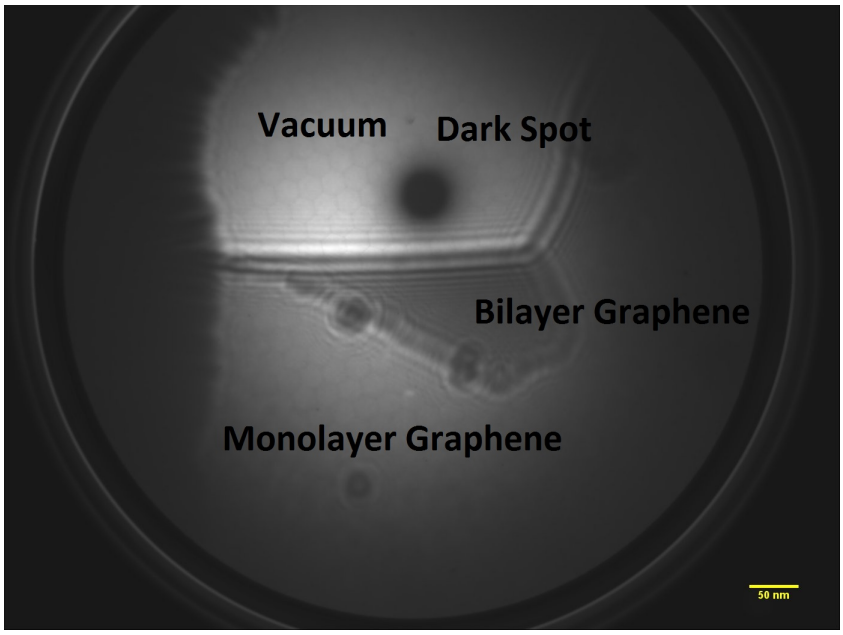

Figure 4.9: A graphene edge experiment at d=1.8 μm, D=70 mm and λ=1.1 Å. The lighter region is the vacuum and the darker region is graphene.

Tip	λ (Å)	Opening Angle (°)	Resolution (Å)
Mutus[11]	1.26	3.83	9.4
SW11	1.07	2.71	11.3

Table 4.1: Comparing the width of holograms with similar values of energy and magnification for W(111) and W(110) [11]. The results for Mutus show an equivalent resolution.

Mutus image was also at a higher magnification than the image collected in this study. The fringes will be easier to detect at higher magnifications because of their increased width.

4.2.1 Graphene Contamination

During the exploration of graphene knife edges, small ciruclar diffraction patterns were visible. These patterns had a tendency to appear near the interface between single and multilayer graphene and were distinguished by their relative transprancies. Reconstructions of the patterns were outsourced to Kreuzer and his student John Sampson at Dalhousie University in Halifax, Canada. The Kreuzer group has a wealth of experience dealing with reconstructions of optical holograms, which allowed initial reconstructions to yield surprising results. The circular patterns revealed small 1-10 nm-sized globular clusters on graphene's surface. Figure 4.10a shows an example of a reconstruction. The contaminants tend to aggregate near the interface between the layers of graphene. The resolution of the image is found to be 1.5 nm. The Kreuzer group provided a number of artificially zoomed images of each individual cluster (figure 4.10b).

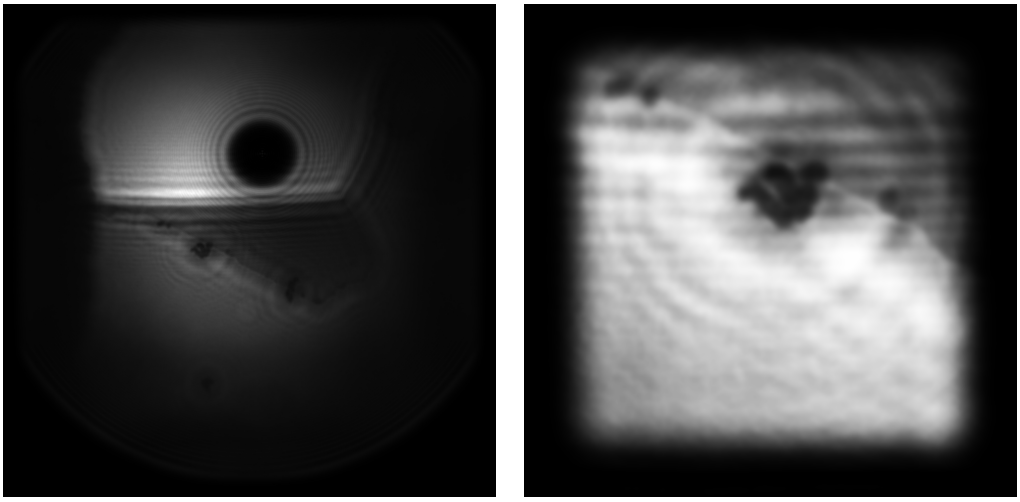

(a) (b)

Figure 4.10: a) A reconstruction of a graphene edge experiment at d=1.8 μm, D=70 mm and λ=1.1 Å. b) A zoomed in version of one of the features in a). It can be seen that the size of the features are on the order of 1 nm.

To increase the resolution, the magnification is increased, the scattered wave becomes more dominant and the width of fringes is increased. An increased number of fringes increases the width of the fringe pattern and hence, the image's resolution. Since this sample is thick, estimated to be 1 nm in diametre per cluster element, the reference beam does not pass through. Increasing the magnification also magnifies the fringes, making them easier to see. There are, however, competing processes. As the tip approaches the sample, the voltage must be decreased to keep the current at a safe level for the source. Decreasing the voltage decreases the wavelength and thus the resolution based on the diffraction limit. Approaching too close can also cause interactions between the fields of the tip and sample, which can cause distortions in the electrons' paths. Figure 4.11 shows a highly magnified hologram of such a defect. These contaminants are physisorbed to the surface as a sufficient voltage can cause them to jump around the surface. The jump, recorded by the camera, takes from 0.14 s to 0.28 s as it takes two frames for the contaminant to come to rest. This could also be a number of jumps, which would mean that the move in fact takes less than 0.14 s. A number of edge sharpness measurements are performed to obtain an average value for the image. Table 4.2 shows a summary of the resolution measurements.

The resolution in this image is then 6.8 Å which is the highest recorded resolution in electron holography to date. Since the sample is of unknown size and origin, it is very difficult to pull more insight out of this sample.

A standard sample for measuring resolution for SEM and TEM is the gold on carbon sample. A similar sample could be useful for electron holography in the form of gold clusters on graphene. This study shows that the physisorbed samples are easily moved on the surface with relatively high voltages, which may limit the resolution of the microscope.

Position	Resolution (Å)
1	6.8
2	6.1
3	6.0
4	6.9
5	6.9
6	7.2
7	8.2

Table 4.2: Summary of resolution measurements for a highly magnified contaminant suspended on graphene. The seven measurements are averaged to obtain a final resolution. The areas where the line profiles were taken are shown in figure 4.11

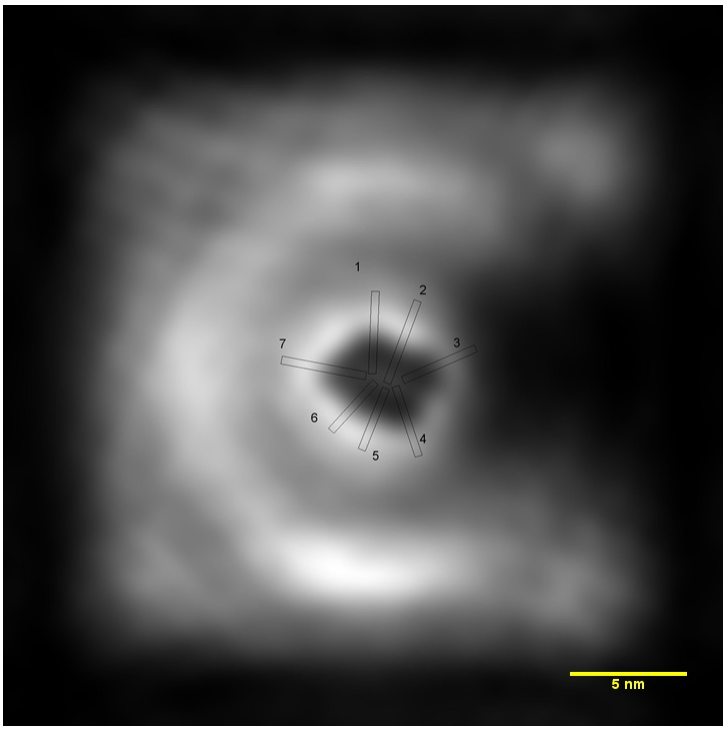

Figure 4.11: Sharpness measurement of a high resolution point defect at d= 180 nm, D= 70 mm and λ= 1.3 Å. To calculate the resolution, an average of seven measurements are taken. The seven profiles are binned using a 20 pixel thick line. The final resolution attained was 6.8 Å. The individual line profiles can be seen in figure 4.12.

Large clusters, more difficult to move, may provide a better measure of the resolution as the voltage could be increased. Studying this effect with a simulation could greatly aid in the synthesis of samples for PPM.

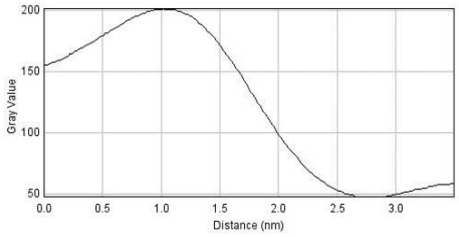

(a) Line profile 1.

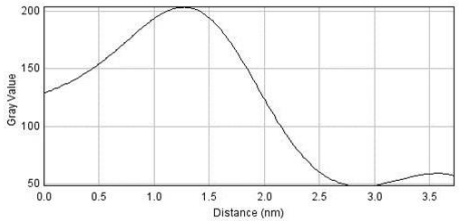

(b) Line profile 2.

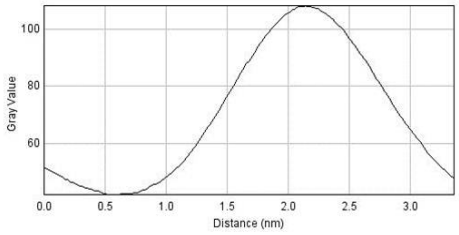

(c) Line profile 3.

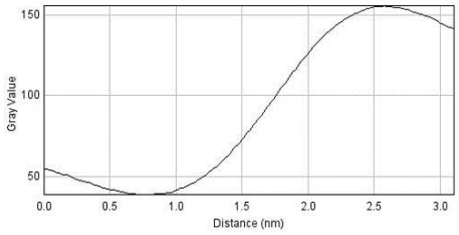

(d) Line profile 4.

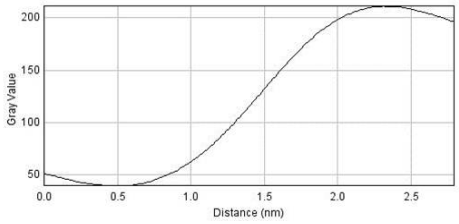

(e) Line profile 5.

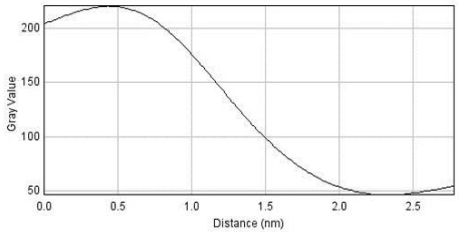

(f) Line profile 6.

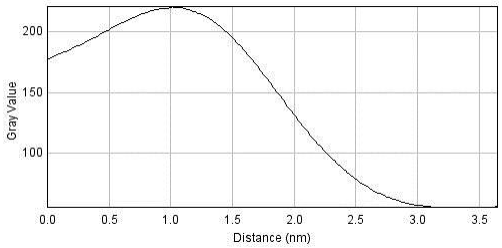

(g) Line profile 7.

Figure 4.12: Line profiles used for the high resolution defect measurement.

Chapter 5

Conclusions and Future Work

A PPM, the simplest possible microscope, is free of lens-induced aberrations and thus is only limited by diffraction. Low energy electron holography, an application of a PPM, allows the user to probe small features on the order of nanometers in a non-destructive way. Electron holography is a relatively young technique which holds much promise.

The goal of the research conducted over the last few years was to further the understanding of the field of electron holography. Until recently, in-line electron holography had been limited to filamentous samples which could be supported over holes in a TEM grid. Graphene was identified as a means to support non-filamentous samples as well as create equipotential planes perpendicular to the motion of electrons. The equipotential planes allow for undistorted holograms. Access to TEM grids covered with graphene were limited by the ability to obtain them from our collaborator. To increase the number of samples it became clear that the group would have to prepare their own samples.

Graphene growth can be achieved on many substrates. Copper foils were chosen for their low carbon solubility which leads to highly reproducible monolayer films. First attempts at graphene growth failed due to the copper being oxidized by leaky mass flow controllers. Successful trials began after the flow controllers were replaced with air tight leak valves. Raman spectroscopy of the copper samples provided evidence of graphitic carbon on the foils. In order to be properly characterized, in terms of layers and quality of the sheet, graphene needed to be transfered to a SiO_2 substrate or TEM grid.

There are many methods which have been suggested for transferring graphene to arbitrary substrates. The most common is the 'wet' technique which uses PMMA to support the graphene layer once the copper has been etched in ammonia persulfate. The graphene is then placed on the arbitrary substrate and the PMMA is dissolved in acetone. Until recently, this step was the limiting factor in this project. Transfers showed islands of disconnected graphene on a SiO_2 substrate. Further sample handling techniques helped improve the coverage of transfers.

Another goal of this research was to streamline the collection and analysis of data. A program, Control, was written such that parts of the microscope could be monitored and

controlled from a central location. The collected data provides insight into measurements for the microscope and the sample. The resolution of the microscope, based on the NA or the virtual source size, can be deduced from this data. The resolution of a holographic microscope is most often measured from the lateral extent of the fringe system in a processed image. Due to the lack of standardization of the minimum requirements for a fringe, this method provides a wide range of possible results. A sharpness measurement, often used in SEM, can provide a standard method of measuring and comparing resolution between subsequent images and microscopes. Further standardization of the resolution measurement can be found in the study of the contrast transfer function (CTF) which describes the microscope's ability to accurately represent the object. The use of the CTF is a common method for measuring the resolution of a TEM microscope. Its application to holography is the subject of further study.

The main difference between this research and research done previously is the source used to create holograms. Previous studies on this microscope have used SATs etched from a polycrystalline wire, W(110). More recent efforts to create SATs using W(111) have shown an increase in etching stability, facilitating the creation of SATs with high aspect ratios which have been shown to have wider opening angles and thus have the capability to probe smaller features (assuming a fully coherent beam). Comparing the two materials in similar ranges of magnification and energy showed that the two materials have a similar coherence angle, 2.97°, but further work is required. The comparison done here is zeroth order in the sense that the magnifications are not identical, and the energies are different. Further steps could be taken to ensure the source is indeed a SAT, as the source sampled here terminated in a trimer. During the characterization of W(111), small circular interference patterns became apparent in the holograms.

After reconstructing these circular interference patterns, it became clear that there were small circular contaminants on the graphene. The size of the contaminants, ≈ 1 nm, provides some potential insight of their composition. Since carbon is a likely contaminant in the system, it is possible that buckey-balls have formed on the surface of graphene. Zooming in on an individual feature of contaminants and reconstructing them shows several small circular contaminants. The resulting resolution of the image using a sharpness measurement is 6.8 Å, the best seen in electron holography to date. The contaminants were physisorbed to the surface of the graphene since they could be caused to move around the surface by increasing the voltage of the source at small tip to sample distances.

Future samples, such as the aforementioned gold on graphene, would be similar to the contaminants on graphene. Would it be possible to fabricate stable nanoparticle samples for observation? The first step would be to create samples of known size, which would reside on suspended graphene drums. A toy model was developed to probe the zeroth order scenario of deposition of gold on a flat vibrating material. The result of the simulation shows that at high enough temperatures and deposition rates creates small nanoparticles which contain

on average 10 atoms which reside near the center of the drum.

5.0.2 Future

Now that graphene can be transfered to TEM grids reproducibly, new exciting samples can be created for observation. Gold on graphene is a sample which would be of great interest due to the high contrast between C and Au. The known size and shape of the gold nanoparticles could also provide insight into the PSF of the system which could allow for the images to be deconvoluted, increasing the overall resolution of the instrument. Graphene can also be used to negate the biprism effect of a CNT, which would facilitate easy reconstructions which have yet to be achieved from this microscope.

To facilitate more insightful data collection, including the reconstruction algorithm in the Control program will provide real time information about the images being captured. Current iterations of the reconstruction algorithm may prove to be too slow to create live images of holograms. Further work on increasing the optimization of the algorithm must be explored.

Another feat unachieved on this microscope is that of three dimensional reconstructions. The difficulty of aligning the sample on the optical axis presents the issue where a reconstructed image will "walk" across the field of view in different planes and become distorted. Figure 5.1 shows a sequence of images of the point defect being reconstructed on many different planes. The images show the walk from right to left as the reconstruction plane approaches the tip. In order to obtain three dimensional recontrustions, a method to estimate this optical axis offset must be developped.

The dark spot created by the opening angle of the tip and the angle of the channels of the MCP is also another issue which needs to be handled. The dark spot is occluding important information about the sample by removing fringes from the hologram. Many different ideas have been suggested to rectify this issue such as increasing the angle of the channels, or creating a special MCP with spherically symmetric channels ensuring that the angle of the electrons never match the channels. Another potential solution to the dark spot problem is to completely eliminate the MCP from the detection mechanism. As it stands, electrons are converted to photons by the phosphor plate which are then converted back into electrons at the CCD camera. Ideally, electrons would be detected directly, removing the intermediate step. Devices, such as the PIXIS camera from Princeton Instruments, is able to detect electrons directly. This, however, would remove the ability to amplify the number of electrons leading to a very low signal. Further research needs to be performed on this subject.

The microscope is not limited to capturing holograms. In a previous dissertation it has been shown that viewing images off the optical axis shows diffraction spots. This technique resembles a well known imaging method called low electron energy diffraction (LEED). LEED could provide a means of measuring the thickness of the graphene sheet or the strain

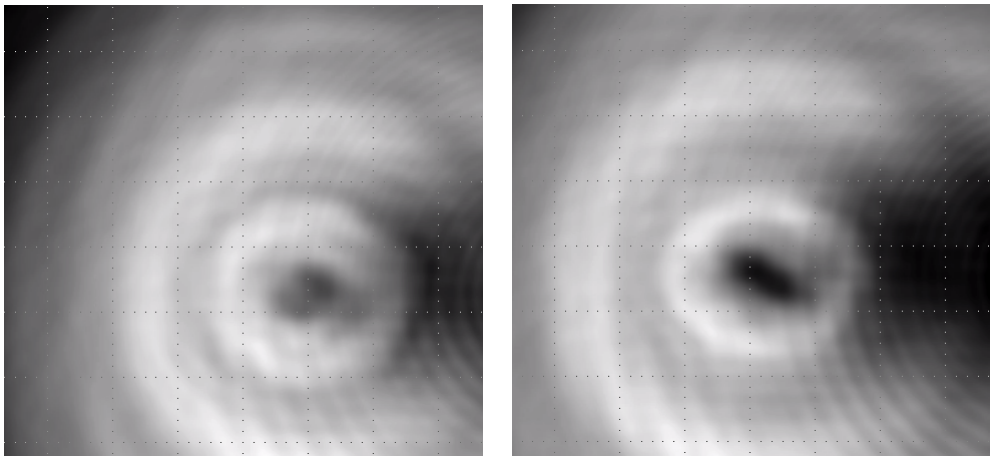

(a)

(b)

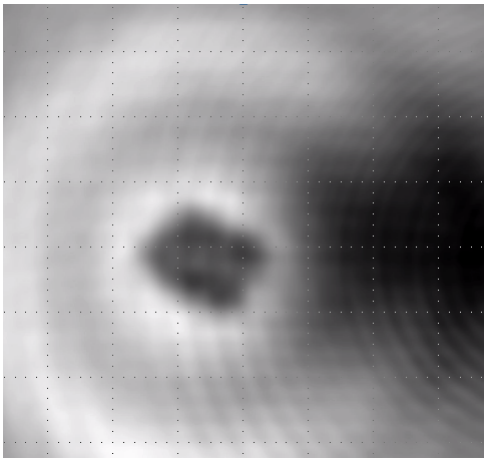

(c)

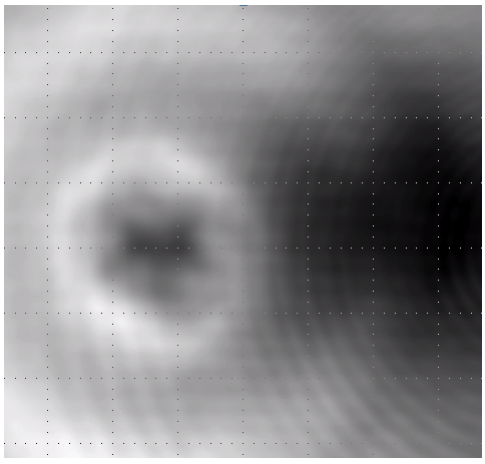

(d)

Figure 5.1: Reconstructions at increasing tip to sample distances for the high resolution contaminant seen in Chapter 4. The contaminant walks from right to left in the 3D reconstruction due to the positional offset of the object from the optical axis.

on the graphene induced by the sample it is supporting.

Electron holography, which has been in development for 60 years, has finally attained tips coherent enough to observe nanoscale features. Further tuning of parameters could lead to breakthrough research of three dimensional reconstructions of samples at the atomic level which would provide insight to many different systems.

Bibliography

[1] Ernst Ruska. Ernst ruska autobiography. *Nobel Foundation*, 1986.

[2] Max Born and Emil Wolf. *Principles of Optics*. Cambridge University Press, 1997.

[3] Sean F. Johnston. *Holographic Visions: A History of New Science*. Oxford University Press, 2006.

[4] Dennis Gabor. A new microscopic principle. *Nature*, 161(4098):777–778, 1948.

[5] Dennis Gabor. Holography, 1948-1971. *Proceedings of the IEEE*, 60(6):655–668, 1972.

[6] Akira Tonomura. *The Quantuum World Unveiled by Electron Waves*. World Scientific, 1998.

[7] AV Crewe, DN Eggenberger, J Wall, and LM Welter. Electron gun using a field emission source. *Review of Scientific Instruments*, 39(4):576–583, 1968.

[8] Hans-Werner Fink. Mono-atomic tips for scanning tunneling microscopy. *IBM journal of research and development*, 30(5):460–465, 1986.

[9] Mathieu Dumberry. Fundamentals of elasticity theory and seismic waves.

[10] MP Silverman, Wayne Strange, and JCH Spence. The brightest beam in science: new directions in electron microscopy and interferometry. *American Journal of Physics*, 63:800–813, 1995.

[11] Josh Mutus. *Low-energy electron point source microscopy and electron holography*. Ph.D. Thesis, 2012.

[12] Dennis Gabor. Improvements in and relating to microscopy, 1952.

[13] Lucian Livadaru, Josh Mutus, and Robert A Wolkow. In-line holographic electron microscopy in the presence of external magnetic fields. *Ultramicroscopy*, 108(5):472–480, 2008.

[14] CJ Powell. Attenuation lengths of low-energy electrons in solids. *Surface science*, 44(1):29–46, 1974.

[15] Raymond F Egerton, Feng Wang, and Peter A Crozier. Beam-induced damage to thin specimens in an intense electron probe. *Microscopy and Microanalysis*, 12(1):65–71, 2006.

[16] R Nave. The rayleigh criterion.

[17] GW Webb, IV Minin, and OV Minin. Variable reference phase in diffractive antennas: Review, applications, new results. *Antennas and Propagation Magazine, IEEE*, 53(2):77–94, 2011.

[18] Grant R Fowles. *Introduction to modern optics*. DoverPublications. com, 1975.

[19] Patrick Michael Whelan, Michael John Hodgson, and T Robinson. *Essential principles of physics*. John Murray, 1987.

[20] Hans-Werner Fink, Heinz Schmid, Eugen Ermantraut, and Torsten Schulz. Electron holography of individual dna molecules. *JOSA A*, 14(9):2168–2172, 1997.

[21] Matthias Germann, Tatiana Latychevskaia, Conrad Escher, and Hans-Werner Fink. Nondestructive imaging of individual biomolecules. *Phys. Rev. Lett.*, 104:095501, Mar 2010.

[22] GB Stevens. Resolving power of lens-less low energy electron point source microscopy. *Journal of Microscopy*, 235(1):9–24, 2009.

[23] JY Mutus, L Livadaru, JT Robinson, R Urban, MH Salomons, M Cloutier, and RA Wolkow. Low-energy electron point projection microscopy of suspended graphene, the ultimate'microscope slide'. *New Journal of Physics*, 13(6):063011, 2011.

[24] Andre K Geim and Konstantin S Novoselov. The rise of graphene. *Nature materials*, 6(3):183–191, 2007.

[25] KS Novoselov, VI Fal, L Colombo, PR Gellert, MG Schwab, K Kim, et al. A roadmap for graphene. *Nature*, 490(7419):192–200, 2012.

[26] M Dragoman, D Dragoman, and AA Muller. High frequency devices based on graphene. In *Semiconductor Conference, 2007. CAS 2007. International*, volume 1, pages 53–56. IEEE, 2007.

[27] Tomás Palacios, Allen Hsu, and Han Wang. Applications of graphene devices in rf communications. *Communications Magazine, IEEE*, 48(6):122–128, 2010.

[28] Melinda Y Han, Barbaros Özyilmaz, Yuanbo Zhang, and Philip Kim. Energy band-gap engineering of graphene nanoribbons. *Physical review letters*, 98(20):206805, 2007.

[29] Yuanbo Zhang, Tsung-Ta Tang, Caglar Girit, Zhao Hao, Michael C Martin, Alex Zettl, Michael F Crommie, Y Ron Shen, and Feng Wang. Direct observation of a widely tunable bandgap in bilayer graphene. *Nature*, 459(7248):820–823, 2009.

[30] Ovidiu Cretu, Arkady V Krasheninnikov, Julio A Rodríguez-Manzo, Litao Sun, Risto M Nieminen, and Florian Banhart. Migration and localization of metal atoms on strained graphene. *Physical review letters*, 105(19):196102, 2010.

[31] Yanqing Wu, Yu-ming Lin, Ageeth A Bol, Keith A Jenkins, Fengnian Xia, Damon B Farmer, Yu Zhu, and Phaedon Avouris. High-frequency, scaled graphene transistors on diamond-like carbon. *Nature*, 472(7341):74–78, 2011.

[32] J Scott Bunch, Scott S Verbridge, Jonathan S Alden, Arend M van der Zande, Jeevak M Parpia, Harold G Craighead, and Paul L McEuen. Impermeable atomic membranes from graphene sheets. *Nano letters*, 8(8):2458–2462, 2008.

[33] Evelyn N Wang and Rohit Karnik. Water desalination: Graphene cleans up water. *Nature Nanotechnology*, 7(9):552–554, 2012.

[34] Shouh Hwang, Che-Cheng Chang, Chien-Hung Lu, Shih-Chin Liu, Yuan-Chih Chang, Ting-Kuo Lee, Horng-Tay Jeng, Hong-Shi Kuo, Chun-Yueh Lin, Chia-Seng Chang, et al. Investigation of single-walled carbon nanotubes with a low-energy electron point projection microscope. *New Journal of Physics*, 15(4):043015, 2013.

[35] Josh Y Mutus, Lucian Livadaru, Radovan Urban, Jason Pitters, A Peter Legg, Mark H Salomons, Martin Cloutier, and Robert A Wolkow. Nanoscale structuring of tungsten tip yields most coherent electron point-source. *New Journal of Physics*, 15(7):073038, 2013.

[36] Dario Braga, Alberto Ripamonti, Diego Savoia, Claudio Trombini, and Achille Umani-Ronchi. Graphite lamellar compounds. a new route to transition metal intercalates. *J. Chem. Soc., Chem. Commun.*, (21):927–928, 1978.

[37] H Estrade-Szwarckopf and BUPS Rousseau. Ups and xps studies of alkali-graphite intercalation compounds. *Synthetic Metals*, 23(1):191–198, 1988.

[38] MS Dresselhaus and G Dresselhaus. Intercalation compounds of graphite. *Advances in Physics*, 30(2):139–326, 1981.

[39] Andre K Geim. Nobel lecture: random walk to graphene. *Reviews of Modern Physics*, 83(3):851, 2011.

[40] K. S. Novoselov, A. K. Geim, S. V. Morozov, D. Jiang, Y. Zhang, S. V. Dubonos, I. V. Grigorieva, and A. A. Firsov. Electric field effect in atomically thin carbon films. *Science*, 306(5696):666–669, 2004.

[41] Tao Peng, Haifeng Lv, Daping He, Mu Pan, and Shichun Mu. Direct transformation of amorphous silicon carbide into graphene under low temperature and ambient pressure. *Scientific reports*, 3, 2013.

[42] Zhen-Yu Juang, Chih-Yu Wu, Chien-Wei Lo, Wei-Yu Chen, Chih-Fang Huang, Jenn-Chang Hwang, Fu-Rong Chen, Keh-Chyang Leou, and Chuen-Horng Tsai. Synthesis of graphene on silicon carbide substrates at low temperature. *Carbon*, 47(8):2026–2031, 2009.

[43] G Nandamuri, S Roumimov, and R Solanki. Chemical vapor deposition of graphene films. *Nanotechnology*, 21(14):145604, 2010.

[44] Congqin Miao, Churan Zheng, Owen Liang, and Ya-Hong Xie. *Physics and Applications of Graphene - Experiments*. InTech, 2011.

[45] Alfonso Reina, Xiaoting Jia, John Ho, Daniel Nezich, Hyungbin Son, Vladimir Bulovic, Mildred S Dresselhaus, and Jing Kong. Large area, few-layer graphene films on arbitrary substrates by chemical vapor deposition. *Nano letters*, 9(1):30–35, 2008.

[46] MT Marques, JB Correia, and O Conde. Carbon solubility in nanostructured copper. *Scripta materialia*, 50(7):963–967, 2004.

[47] M Nakamizo, R Kammereck, and P Letal Walker. Laser raman studies on carbons. *Carbon*, 12(3):259–267, 1974.

[48] AC Ferrari, JC Meyer, V Scardaci, C Casiraghi, Michele Lazzeri, Francesco Mauri, S Piscanec, Da Jiang, KS Novoselov, S Roth, et al. Raman spectrum of graphene and graphene layers. *Physical review letters*, 97(18):187401, 2006.

[49] W-H Soe, AM Shikin, F Moresco, VK Adamchuk, and K-H Rieder. Hreels investigation of graphite monolayer stripes formed on stepped ni (771). *Physical Review B*, 64(23):235404, 2001.

[50] Recep Zan, Chris Muryn, Ursel Bangert, Philip Mattocks, Paul Wincott, David Vaughan, Xuesong Li, Luigi Colombo, Rodney S Ruoff, Bruce Hamilton, et al. Scanning tunnelling microscopy of suspended graphene. *Nanoscale*, 4(10):3065–3068, 2012.

[51] L Zhao, KT Rim, H Zhou, R He, TF Heinz, A Pinczuk, GW Flynn, and AN Pasupathy. The atomic-scale growth of large-area monolayer graphene on single-crystal copper substrates. *arXiv preprint arXiv:1008.3542*, 2010.

[52] P Blake, EW Hill, AH Castro Neto, KS Novoselov, D Jiang, R Yang, TJ Booth, and AK Geim. Making graphene visible. *Applied Physics Letters*, 91:063124, 2007.

[53] Yung-Chang Lin, Chun-Chieh Lu, Chao-Huei Yeh, Chuanhong Jin, Kazu Suenaga, and Po-Wen Chiu. Graphene annealing: how clean can it be? *Nano letters*, 12(1):414–419, 2011.

[54] William Regan, Nasim Alem, Benjamín Alemán, Baisong Geng, Caglar Girit, Lorenzo Maserati, Feng Wang, Michael Crommie, and A Zettl. A direct transfer of layer-area graphene. *Applied Physics Letters*, 96(11):113102–113102, 2010.

[55] Xuesong Li, Carl W Magnuson, Archana Venugopal, Rudolf M Tromp, James B Hannon, Eric M Vogel, Luigi Colombo, and Rodney S Ruoff. Large-area graphene single crystals grown by low-pressure chemical vapor deposition of methane on copper. *Journal of the American Chemical Society*, 133(9):2816–2819, 2011.

[56] EE Martin, JK Trolan, and WP Dyke. Stable, high density field emission cold cathode. *Journal of Applied Physics*, 31(5):782–789, 1960.

[57] Radovan Urban, Jason L. Pitters, and Robert A. Wolkow. Gas field ion source current stability for trimer and single atom terminated w(111) tips. *Applied Physics Letters*, 100(26):263105, 2012.

[58] Jason L. Pitters, Radovan Urban, and Robert A. Wolkow. Creation and recovery of a w(111) single atom gas field ion source. *The Journal of Chemical Physics*, 136(15):154704, 2012.

[59] MLT Chae Postek and András E Vladár. Image sharpness measurement in scanning electron microscopypart i. *Scanning*, 20(1):1–9, 1998.

[60] JB Tiller, A Barty, D Paganin, and KA Nugent. The holographic twin image problem: a deterministic phase solution. *Optics communications*, 183(1):7–14, 2000.

[61] Tatiana Latychevskaia and Hans-Werner Fink. Solution to the twin image problem in holography. *Physical review letters*, 98(23):233901, 2007.